

First comprehensive measurement of spin observables and differential cross sections $d\sigma/dt$ in ω photoproduction off the proton for $2.7 < E_\gamma < 5.2$ GeV using CLAS

T. Hu,¹⁴ Z. Akbar,^{14,*} V. Crede,^{14,†} J. M. Laget,⁴³ V. Mathieu,^{54,55} M. J. Amaryan,³⁵ W. R. Armstrong,¹ H. Atac,⁴² N. A. Baltzell,^{41,43} L. Barion,¹⁷ M. Battaglieri,¹⁹ I. Bedlinskiy,³⁰ B. Benkel,⁴⁴ F. Benmokhtar,¹⁰ A. Bianconi,^{23,45} L. Biondo,^{19,22,46} A. Biselli,¹¹ M. Bondi,¹⁹ F. Bossù,⁶ S. Boiarinov,⁴³ W. J. Briscoe,¹⁵ S. Bueltmann,³⁵ D. Bulumulla,³⁵ V. D. Burkert,⁴³ R. Capobianco,⁸ D. S. Carman,⁴³ J. C. Carvajal,¹³ A. Celentano,¹⁹ T. Chetry,²⁹ G. Ciullo,^{12,17} G. Clash,⁴⁹ P. L. Cole,²⁷ M. Contalbrigo,¹⁷ G. Costantini,^{23,45} A. D'Angelo,^{20,39} N. Dashyan,⁵³ R. De Vita,¹⁹ M. Defurne,⁶ A. Deur,⁴³ S. Diehl,^{8,36} C. Djalali,^{34,41} R. Dupre,²⁴ H. Egiyan,^{31,43} A. El Alaoui,⁴⁴ L. El Fassi,^{1,29} L. Elouadrhiri,⁴³ P. Eugenio,¹⁴ S. Fegan,⁴⁹ A. Filippi,²¹ G. Gavalian,^{35,43} Y. Ghazilyan,⁵³ G. P. Gilfoyle,³⁸ F. X. Girod,⁴³ A. A. Golubenko,⁴⁰ G. Gosta,^{23,45} R. W. Gothe,⁴¹ K. A. Griffioen,⁵² M. Guidal,²⁴ K. Hafidi,¹ H. Hakobyan,^{44,53} M. Hattaway,³⁵ T. B. Hayward,⁸ D. Heddle,^{7,43} A. Hobart,²⁴ M. Holtrop,³¹ Y. Ilieva,^{15,41} D. G. Ireland,⁴⁸ E. L. Isupov,⁴⁰ D. Jenkins,⁵⁰ H. S. Jo,²⁶ K. Joo,⁸ S. Joosten,¹ D. Keller,⁵¹ A. Khanal,¹³ M. Khandaker,^{33,‡} A. Kim,⁸ W. Kim,²⁶ F. J. Klein,⁵ V. Klimenko,⁸ A. Kripko,³⁶ V. Kubarovskiy,^{37,43} V. Lagerquist,³⁵ L. Lanza,²⁰ M. Leali,^{23,45} P. Lenisa,^{12,17} K. Livingston,⁴⁸ I. J. D. MacGregor,⁴⁸ D. Marchand,²⁴ L. Marsicano,¹⁹ V. Mascagna,^{23,45} M. E. McCracken,⁴ B. McKinnon,⁴⁸ Z. E. Meziani,¹ S. Migliorati,^{23,45} R. G. Milner,²⁸ T. Mineeva,^{8,44} M. Mirazita,¹⁸ V. Mokeev,⁴³ C. Munoz Camacho,²⁴ P. Nadel-Turronski,⁴³ K. Neupane,⁴¹ J. Newton,⁴³ S. Niccolai,²⁴ M. Nicol,⁴⁹ G. Niculescu,²⁵ M. Osipenko,¹⁹ A. I. Ostrovidov,¹⁴ P. Pandey,³⁵ M. Paolone,³² L. L. Pappalardo,^{12,17} R. Paremuzyan,⁴³ E. Pasyuk,⁴³ S. J. Paul,⁴⁷ W. Phelps,⁷ N. Pilleux,²⁴ O. Pogorelko,³⁰ J. W. Price,² Y. Prok,^{35,51} B. A. Raue,¹³ T. Reed,¹³ M. Ripani,¹⁹ J. Ritman,¹⁶ A. Rizzo,^{20,39} G. Rosner,⁴⁸ F. Sabatié,⁶ C. Salgado,³³ S. Schadmand,¹⁶ A. Schmidt,¹⁵ R. A. Schumacher,⁴ E. V. Shirokov,⁴⁰ U. Shrestha,⁸ P. Simmerling,⁸ D. Sokhan,^{6,48} N. Sparveris,⁴² S. Stepanyan,⁴³ I. I. Strakovsky,¹⁵ S. Strauch,⁴¹ R. Tyson,⁴⁸ M. Ungaro,^{8,43} L. Venturelli,^{23,45} H. Voskanyan,⁵³ A. Vossen,^{9,43} E. Voutier,²⁴ D. P. Watts,⁴⁹ X. Wei,⁴³ M. H. Wood,^{3,41} B. Yale,⁵² M. Yurov,²⁶ N. Zachariou,⁴⁹ and J. Zhang^{35,51}

(CLAS Collaboration at Jefferson Laboratory)

¹Argonne National Laboratory, Argonne, Illinois 60439, USA

²California State University, Dominguez Hills, Carson, CA 90747, USA

³Canisius College, Buffalo, NY 14208, USA

⁴Carnegie Mellon University, Pittsburgh, Pennsylvania 15213, USA

⁵Catholic University of America, Washington, DC 20064, USA

⁶IRFU, CEA, Université Paris-Saclay, F-91191 Gif-sur-Yvette, France

⁷Christopher Newport University, Newport News, Virginia 23606, USA

⁸University of Connecticut, Storrs, Connecticut 06269, USA

⁹Duke University, Durham, North Carolina 27708-0305, USA

¹⁰Duquesne University, 600 Forbes Avenue, Pittsburgh, PA 15282, USA

¹¹Fairfield University, Fairfield, Connecticut 06482, USA

¹²Università di Ferrara, 44121 Ferrara, Italy

¹³Florida International University, Miami, Florida 33199, USA

¹⁴Florida State University, Tallahassee, Florida 32306, USA

¹⁵The George Washington University, Washington, DC 20052, USA

¹⁶GSI Helmholtzzentrum für Schwerionenforschung GmbH, D-64291 Darmstadt, Germany

¹⁷INFN, Sezione di Ferrara, 44100 Ferrara, Italy

¹⁸INFN, Laboratori Nazionali di Frascati, 00044 Frascati, Italy

¹⁹INFN, Sezione di Genova, 16146 Genova, Italy

²⁰INFN, Sezione di Roma Tor Vergata, 00133 Rome, Italy

²¹INFN, Sezione di Torino, 10125 Torino, Italy

²²INFN, Sezione di Catania, 95123 Catania, Italy

²³INFN, Sezione di Pavia, 27100 Pavia, Italy

²⁴Université Paris-Saclay, CNRS/IN2P3, IJCLab, 91405 Orsay, France

²⁵James Madison University, Harrisonburg, Virginia 22807, USA

²⁶Kyungpook National University, Daegu 41566, Republic of Korea

²⁷Lamar University, 4400 MLK Blvd, PO Box 10046, Beaumont, Texas 77710, USA

²⁸Massachusetts Institute of Technology, Cambridge, Massachusetts 02139-4307, USA

²⁹Mississippi State University, Mississippi State, MS 39762-5167, USA

³⁰National Research Centre Kurchatov Institute - ITEP, Moscow, 117259, Russia

³¹University of New Hampshire, Durham, New Hampshire 03824-3568, USA

³²New Mexico State University, PO Box 30001, Las Cruces, NM 88003, USA

- ³³*Norfolk State University, Norfolk, Virginia 23504, USA*
³⁴*Ohio University, Athens, Ohio 45701, USA*
³⁵*Old Dominion University, Norfolk, Virginia 23529, USA*
³⁶*II Physikalisches Institut der Universität Gießen, 35392 Gießen, Germany*
³⁷*Rensselaer Polytechnic Institute, Troy, New York 12180-3590, USA*
³⁸*University of Richmond, Richmond, Virginia 23173, USA*
³⁹*Università di Roma Tor Vergata, 00133 Rome Italy*
⁴⁰*Department of Physics and Skobeltsyn Institute of Nuclear Physics,
Lomonosov Moscow State University, 119234 Moscow, Russia*
⁴¹*University of South Carolina, Columbia, South Carolina 29208, USA*
⁴²*Temple University, Philadelphia, PA 19122, USA*
⁴³*Thomas Jefferson National Accelerator Facility, Newport News, Virginia 23606, USA*
⁴⁴*Universidad Técnica Federico Santa María, Casilla 110-V Valparaíso, Chile*
⁴⁵*Università degli Studi di Brescia, 25123 Brescia, Italy*
⁴⁶*Università degli Studi di Messina, 98166 Messina, Italy*
⁴⁷*University of California Riverside, 900 University Avenue, Riverside, CA 92521, USA*
⁴⁸*University of Glasgow, Glasgow G12 8QQ, United Kingdom*
⁴⁹*University of York, York YO10 5DD, United Kingdom*
⁵⁰*Virginia Tech, Blacksburg, Virginia 24061-0435, USA*
⁵¹*University of Virginia, Charlottesville, Virginia 22901, USA*
⁵²*College of William and Mary, Williamsburg, Virginia 23187-8795, USA*
⁵³*Yerevan Physics Institute, 375036 Yerevan, Armenia*
⁵⁴*Departamento de Física Teórica, Universidad Complutense de Madrid and IPARCOS, E-28040 Madrid, Spain*
⁵⁵*Departament de Física Quàntica i Astrofísica and Institut de Ciències del Cosmos, Universitat de Barcelona, E-08028, Spain*

(Dated: Received: March 21, 2022/ Revised version:)

We report on the differential cross sections $d\sigma/dt$, the unpolarized spin-density matrix elements ρ_{00}^0 , ρ_{1-1}^0 , $\text{Re } \rho_{10}^0$, and the first extraction of the polarized elements $\text{Im } \rho_{10}^3$, $\text{Im } \rho_{1-1}^3$ for the reaction $\gamma p \rightarrow p\omega$ using the CLAS spectrometer at Jefferson Laboratory. The ω mesons were detected in their dominant charged decay mode, $\omega \rightarrow \pi^+\pi^-\pi^0$, and all t -dependent results are presented in a fine binning for incident photon energies between 2.73 and 5.16 GeV (corresponding to the center-of-mass energy range $W \in [2.45, 3.25]$ GeV). All matrix elements are first measurements for $-t > 0.6$ GeV². Moreover, differential cross sections $d\sigma/d(\cos\Theta)$ and the unpolarized spin-density matrix elements in the Adair frame are presented for the incident photon energy range 1.56–3.80 GeV (corresponding to $W \in [1.95, 2.83]$ GeV). These new ω photoproduction data are consistent with earlier CLAS results but extend the energy range well beyond the nucleon resonance region into the Regge regime. The comparison with Regge-theory-based model predictions shows that the new data impose more stringent constraints on our understanding of ω photoproduction.

PACS numbers: 13.60.Le, 13.60.-r, 14.20.Gk, 25.20.Lj

The light-flavor vector mesons ρ , ω , and ϕ have the same spin, parity and charge conjugation quantum numbers, $J^{PC} = 1^{--}$, as the photon and, therefore, these mesons play an important role in photoproduction. In high-energy ω photoproduction, the non-resonant amplitude is dominated by a diffractive mechanism, whereas single- π exchange has been predicted to dominate in the nucleon resonance regime at lower energies. The contribution from nucleon excitations in ω photoproduction was recently studied by several groups [1–4]. Surprisingly, an amplitude analysis within the Bonn-Gatchina framework [5] found Pomeron-exchange to provide the largest contribution to the non-resonant background. In vector-meson photoproduction, the spin observables of the vector mesons are represented by their density matrix. Its elements, the spin-density matrix elements (SDMEs), are the physical observables that provide information on the underlying production mechanism and the decay distribution, $W(\cos\theta, \phi)$, of the vector me-

son. In Ref. [5], the t -channel amplitude was identified by polarized SDMEs using linear beam polarization, and additional beam- and beam-target polarization observables [6, 7].

At low momentum transfer, the differential cross section exhibits the typical exponential $-t$ dependence expected from Pomeron and Reggeon exchange. This diffractive production mechanism is described by the incident photon that fluctuates into a vector meson and then elastically scatters from the target nucleon. At large momentum transfer, the cross section shows a flat behavior that can be explained in terms of QCD-inspired two-gluon exchange [8]. The impact parameter becomes small enough and prevents the two constituent gluons from forming the exchanged Pomeron. Moreover, the light, non-strange quark composition of the ω meson allows valence quarks to be exchanged between the meson and recoil nucleon [9]. In contrast, the latter mechanism is suppressed in single- ϕ meson photoproduction

by the OZI rule and two-gluon exchange dominates. At medium energies, it is important to establish factorization of Regge vertices to separate mesons from baryons. This has been discussed in a recent Regge-based study that also provides the implication of Regge-pole models on the SDMEs [10].

The low-energy regime close to threshold, where nucleon resonances dominate ω photoproduction, and the Regge regime are analytically connected. However, the scarcity of $-t$ -dependent cross sections and other spin observables has hindered our understanding of the transition from the baryon resonance regime to high-energy photoproduction. Moreover, each Reggeon exchange has a known energy behavior, whereas the dependence on the momentum exchange is initially unknown and only poorly understood in the transition and medium-energy regimes.

In this Letter, we report differential cross sections and various extracted SDMEs for the center-of-mass energy range $W \in [1.95, 3.25]$ GeV for the reaction $\vec{\gamma}p \rightarrow p\omega$ using circularly polarized tagged photons. The $\omega \rightarrow \pi^+\pi^-\pi^0$ decay angular distribution W is parameterized by the density matrices ρ^α , $\alpha = 0, 1, 2, 3$. For circularly polarized incident photons with helicities $\lambda_\gamma = \pm 1$, $W^\pm(\cos\theta, \phi)$ is given by [11]

$$W^\pm(\cos\theta, \phi) = W^0(\cos\theta, \phi) \pm \delta_\odot W^3(\cos\theta, \phi), \quad (1)$$

where δ_\odot denotes the degree of circular beam polarization, and θ and ϕ are the polar and azimuthal angles of the normal to the decay plane ($\hat{k}_{\pi^+} \times \hat{k}_{\pi^-}$) in the ω rest frame. In this analysis, the SDMEs were extracted from the data for each kinematic bin, $(W, \cos\Theta_{c.m.}^\omega)$ or $(W, -t)$, by performing an Extended Maximum Likelihood fit to Eq. (1) with

$$W(\theta, \phi, \rho^0) = \frac{3}{4\pi} \left(\frac{1}{2} (1 - \rho_{00}^0) + \frac{1}{2} (3\rho_{00}^0 - 1) \cos^2\theta \right. \\ \left. - \sqrt{2} \operatorname{Re} \rho_{10}^0 \sin 2\theta \cos \phi - \rho_{1-1}^0 \sin^2 \theta \cos 2\phi \right) \quad (2)$$

$$W(\theta, \phi, \rho^3) = \frac{3}{4\pi} \left(\sqrt{2} \operatorname{Im} \rho_{10}^3 \sin 2\theta \sin \phi \right. \\ \left. + \operatorname{Im} \rho_{1-1}^3 \sin^2 \theta \sin 2\phi \right), \quad (3)$$

where ρ_{00}^0 , ρ_{1-1}^0 , $\operatorname{Re} \rho_{10}^0$ and $\operatorname{Im} \rho_{10}^3$, $\operatorname{Im} \rho_{1-1}^3$ are the unpolarized and polarized SDMEs, respectively.

The differential cross sections $d\sigma/dt$ were initially measured in the 1970s and 1980s at the Stanford Linear Accelerator Center (SLAC) at $E_\gamma = 2.8, 4.7, 9.3$ GeV using a laser-produced polarized photon beam [12, 13] and at the Cornell Laboratory of Nuclear Studies using incident tagged-photons with energies between 7.5 GeV and 10.5 GeV [14]. At the electron synchrotron NINA, Daresbury Laboratory, measurements were made in the

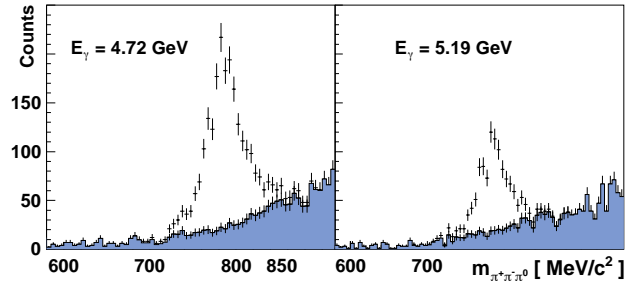


FIG. 1. Examples of signal and background mass distributions from data after applying all kinematic cuts. The invariant $\pi^+\pi^-\pi^0$ masses are shown for approximately 70-MeV-wide E_γ bins with center values of $E_\gamma = 4.72$ GeV (left) and 5.19 GeV (right). See text for details.

photon energy range 2.8 to 4.8 GeV at backward angles [15] and by the LAMP2 Group at forward angles [16]. The LAMP2 group published very wide energy bins. Therefore, these data and earlier statistically limited data from the Cambridge [17] and DESY [18] bubble chamber groups are omitted here. More recently, the CLAS Collaboration at Jefferson Laboratory reported cross section data for four different energy bins between 3.2 and 3.92 GeV [19]. Unpolarized SDMEs were extracted at SLAC [13], Cornell [14], and Daresbury [16] at the above energies for $-t < 0.6$ GeV², by CLAS [20] for $E_\gamma < 3.83$ GeV in a $(E_\gamma, \cos\Theta_{c.m.}^\omega)$ representation, and at ELSA [5] below 2.5 GeV. Our measurements are first measurements for $-t > 0.6$ GeV². Some experiments reported data on SDMEs using linear polarization [5, 13]. The polarized SDMEs presented here have been extracted from photoproduction data using circular polarization; they are also first measurements.

These new results were obtained within the framework of the CLAS-g12 experiment [21], conducted at Jefferson Laboratory before the 12 GeV upgrade. CLAS-g12 used longitudinally polarized electrons with energies of $E_{e^-} = 5.715$ GeV and polarization $\sim 67.2\%$ [22] on a liquid-hydrogen target. Circularly polarized photons were obtained by transferring the polarization from the electrons to the photons in a bremsstrahlung process when the electrons scattered off an amorphous gold radiator. The degree of the photon-beam polarization, δ_\odot , was given as a function of the degree of electron-beam polarization, δ_{e^-} , and the photon-beam energy E_γ as [23]:

$$\delta_\odot = \delta_{e^-} \cdot \frac{4x - x^2}{4 - 4x + 3x^2}, \quad (4)$$

where $x = E_\gamma/E_{e^-}$.

The polarized photons were energy and time tagged with resolutions of 0.1% and 100 ps, respectively, using a photon tagging system [24].

The CLAS detector, with its six-fold symmetry about the beamline (sectors), was capable of detecting charged

particles with a laboratory polar-angle coverage of [8, 142] $^{\circ}$ and almost 2π coverage in the azimuthal angle [25]. The final-state particles traversed several layers of sub-detectors, including drift chambers (DC) and time-of-flight (TOF) scintillators. A start counter (SC) provided the initial time information of the events. For an event to be recorded, the trigger required a scattered electron in the bremsstrahlung tagger in coincidence with either (a) (at least) three charged tracks in different sectors with no restrictions on photon energy, or (b) only two tracks in different sectors with the additional requirement of at least one tagger photon with an energy above 3.6 GeV.

In this analysis, the ω was reconstructed from its $\pi^+\pi^-\pi^0$ decay with a branching ratio of $(89.3 \pm 0.6)\%$ [26]. The selection of the $p\pi^+\pi^-\pi^0$ sample is outlined in Ref. [21]. In this procedure, events were selected to have exactly one incident-photon candidate with a timing (using the photon tagger) at the event vertex within 1 ns of the event time provided by the SC. Only those events that had exactly one proton, π^+ , and π^- were retained. To further improve the particle identification, each particle's β value was calculated separately from its measured momentum using the DC, β_{DC} , and from its measured velocity using the TOF system and the SC, β_{TOF} . Events were selected based on good agreement of β_{DC} and β_{TOF} [21]. The momenta of the final-state particles were corrected for energy losses using standard CLAS techniques.

A four-constraint (4C) kinematic fit to the exclusive $\gamma p \rightarrow p\pi^+\pi^-$ reaction imposing energy and momentum conservation aided in tuning the full covariance matrix. The reaction $\gamma p \rightarrow p\pi^+\pi^-$ (missing π^0) was then kinematically fit, and events with a confidence level below 0.01 were rejected, removing most of the $\pi^+\pi^-$ background. In a final step, the remaining background beneath the ω peak was accounted for using a multivariate side-band subtraction technique [27], which determined the probability Q for an event to be a signal event (as opposed to background) on the basis of a sample of its nearest kinematic neighbors in a very small region of the multi-dimensional $\pi^+\pi^-\pi^0$ phase space around the candidate event [21, 27]. The method assumes that the signal and background distributions do not vary rapidly in the selected region. The $\pi^+\pi^-\pi^0$ mass distribution of each event and its nearest kinematic neighbors was fit using a Johnson form for the signal probability function (PDF) and a second-order Chebychev polynomial for the background PDF. The value of Q was then defined as the ratio of signal to total amplitude at the mass of the candidate event. Figure 1 demonstrates the quality of the background subtraction. Examples of signal and background distributions are shown in the invariant $\pi^+\pi^-\pi^0$ mass obtained by weighting each event with Q and $1-Q$, respectively. Likewise, in this analysis, event yields for cross section measurements were based on sums over Q values,

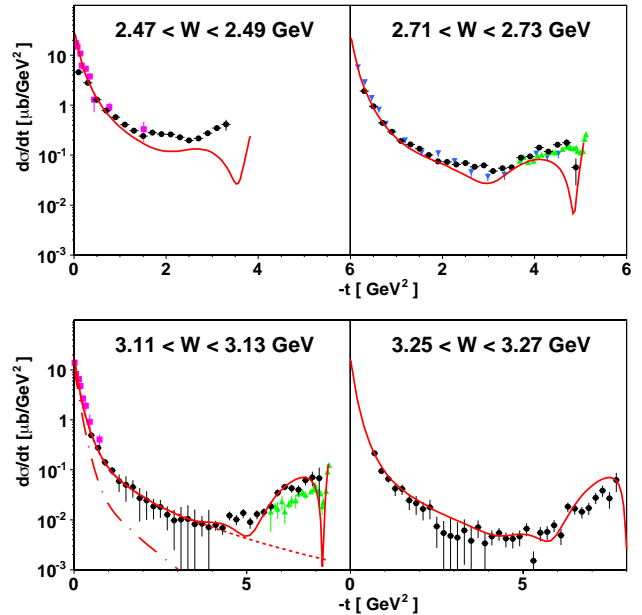


FIG. 2. Four selected examples of $d\sigma/dt$ in 20-MeV-wide center-of-mass bins. The new CLAS data are shown as the black solid circles (\bullet) and the uncertainties include the statistical and Q -value correlation uncertainties added in quadrature. The remaining energy bins for the entire W range 2.45–3.25 GeV are also available [29]. Also shown for comparison are earlier data from CLAS [19] (\blacktriangledown) for the energy bin $E_\gamma \in [3.38, 3.56]$ GeV, (all published data below 6 GeV from) NINA [15] (\blacktriangle) at $E_\gamma = 3.5$ GeV and 4.7 GeV, and SLAC [13] (\blacksquare) at $E_\gamma = 2.8$ GeV and 4.7 GeV. In these energy bins, $\Theta_{\text{c.m.}}^\omega = 90^\circ (180^\circ)$ corresponds to $-t = 1.92, 2.54, 3.68, 4.08$ GeV 2 (3.82, 5.07, 7.37, 8.16 GeV 2), respectively. The red curves denote the model predictions of Ref. [33]: full solution (solid curve), only two-gluon and f_2 contributions (long dash-dotted curve), additional π exchange (dashed line).

whereas contributions to the decay angular distribution given by Eq. (1) have been weighted event-by-event with the corresponding Q values to subtract background.

The $\gamma p \rightarrow p\omega \rightarrow p\pi^+\pi^-\pi^0$ acceptance of CLAS was evaluated in GEANT3 [28] Monte-Carlo simulations by generating events evenly distributed across the available phase space. The Monte Carlo events were then analyzed using the same reconstruction and selection criteria that were applied to the data events [21].

The differential ω photoproduction cross section as a function of $-t$ is shown in Fig. 2 for four selected energy bins. The horizontal bars reflect the bin size. The full set of cross sections $d\sigma/d(\cos\Theta)$ in 20-MeV-wide and 10-MeV-wide bins for the W range 1.95–2.35 GeV and 2.35–2.83 GeV, respectively, and $d\sigma/dt$ in 20-MeV-wide bins for the W range 2.45–3.25 GeV is provided as supplemental material [29]. A ratio distribution of CLAS-g11a [20] and our new CLAS-g12 results using the $d\sigma/d(\cos\Theta)$ cross sections shows a fairly Gaussian

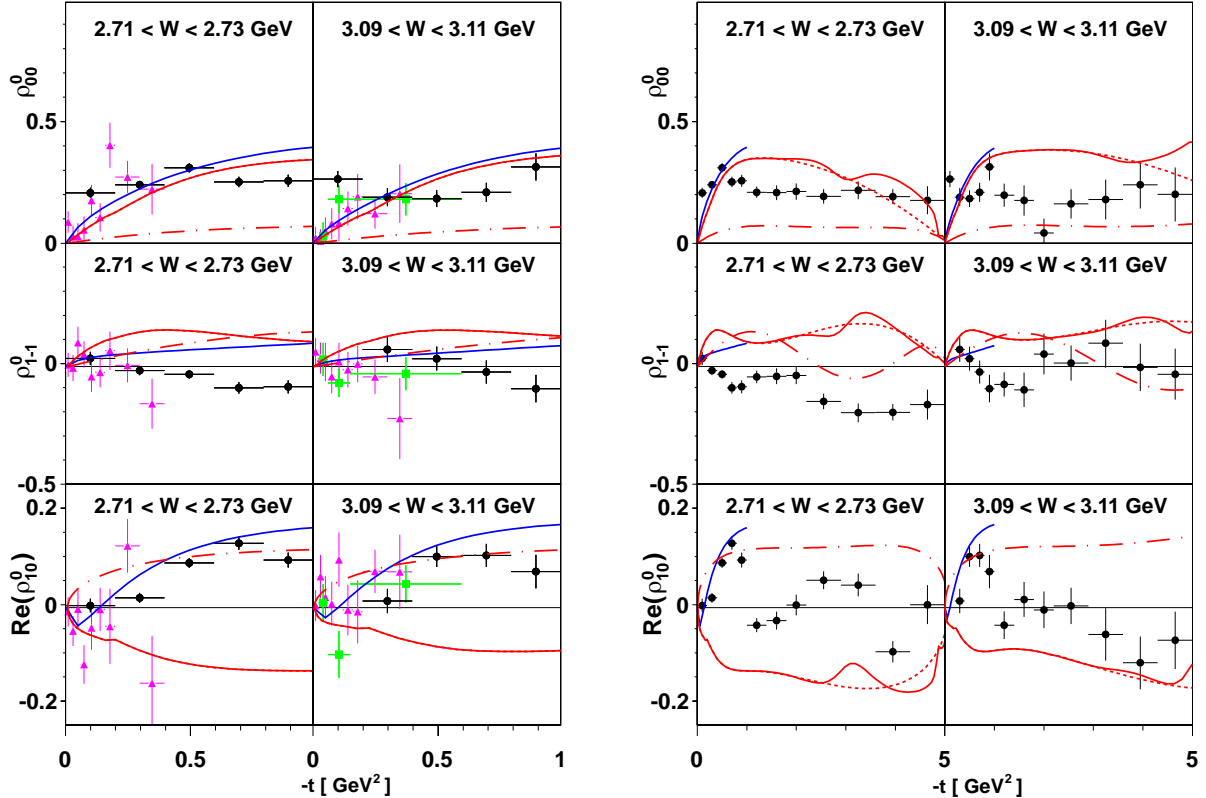


FIG. 3. Examples of the three unpolarized SDMEs ρ_{00}^0 (top), $\text{Re}(\rho_{10}^0)$ (middle), ρ_{1-1}^0 (bottom) in the helicity frame. The new CLAS data are shown as the black solid circles (\bullet). The remaining energy bins for the entire W range 2.45–3.25 GeV are also available [31]. On the left, the three elements are shown for $0 < -t < 1 \text{ GeV}^2$ to allow for better comparison with previously published results from SLAC [13] (\blacksquare) at $W \approx 3.11 \text{ GeV}$ and LAMP2 [16] (\blacktriangle) at $W \approx 2.8 \text{ GeV}$ and $W \approx 3.1 \text{ GeV}$. On the right, the new results are shown for $0 < -t < 5 \text{ GeV}^2$. The blue curves denote the model prediction of Ref. [10]; see caption of Fig. 2 for the red curves of Ref. [33].

distribution, which indicates that an overall decrease of about 1.2% is observed in these new data relative to the previous CLAS data. The earlier CLAS-g6 results [19] shown in Fig. 2 are also in excellent agreement with these new results. Data from NINA at large momentum transfer [15] underestimate the new CLAS results by about 25%. In the region $-t < 1 \text{ GeV}^2$, good agreement is observed with the previous SLAC measurements [13]. The $d\sigma/dt$ cross sections show the expected exponential Ae^{Bt} behavior for $0.1 < -t < 0.5 \text{ GeV}^2$. We have determined $B = 4.6 \pm 0.2 \text{ GeV}^{-2}$ and $B = 4.1 \pm 0.3 \text{ GeV}^{-2}$ for $W = 2.48 \text{ GeV}$ and 2.72 GeV , respectively. These values are consistent with the CLAS measurements of Ref. [19].

A major contribution to the overall systematic uncertainty comes from the background subtraction (see details in Refs. [21, 27]). This absolute contribution is added in quadrature to the statistical uncertainty and shown for each data point in Fig. 2. Additional scale-type systematic uncertainties originate from modeling the detector acceptance (7.1%) [21, 30], kinematic fitting (1.2%), trigger efficiency correction (1.1%), liquid-

hydrogen density (0.5%) [30], photon flux normalization (5.7%) [30], and the $\omega \rightarrow \pi^+ \pi^- \pi^0$ branching fraction (0.6%) [26].

For each $(W, \cos \Theta_{\text{c.m.}}^\omega)$ and $(W, -t)$ bin, an event-based maximum-likelihood technique was applied to fit Eq. (1) to the two-dimensional ω decay angular distribution spanned by the two angles of the normal to the three-pion plane in the ω rest frame. The analysis was performed in both the helicity and the Adair frames. Examples of the three unpolarized SDMEs are shown in Fig. 3 (left) for two selected 20-MeV-wide W bins and $-t < 1 \text{ GeV}^2$ to facilitate comparison with previous results. The full $-t$ range for these two W bins is shown in Fig. 3 (right) and for the two polarized SDMEs in Fig. 4. The full set of SDMEs from this analysis is available in Ref. [31]. Systematic uncertainties were determined for all SDMEs by modifying each Q factor by its corresponding fit uncertainty σ_Q and re-extracting the observables. The absolute difference was taken as the systematic uncertainty and added in quadrature to the statistical uncertainty.

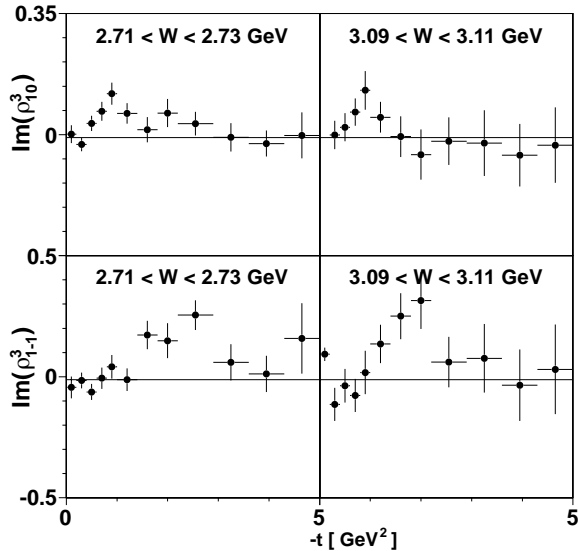


FIG. 4. Examples of the two polarized SDMEs $\text{Im}(\rho_{10}^3)$ and $\text{Im}(\rho_{1-1}^3)$ in the helicity frame for the same two energy bins presented in Fig. 3. The remaining energy bins for the entire W range 2.45–3.25 GeV are also available [31]. These results are first measurements and therefore, a model description is not yet provided.

The Regge-based model of Ref. [10] was developed to understand SDMEs in light vector-meson photoproduction and to study the $\gamma - \omega$ vertex. In the model, the Reggeon amplitude factorizes into a product of two vertices, which describe the photon and proton interactions. This factorization follows from unitarity in the t channel and allows for the study of the helicity structure at the photon vertex independently from the target. In the center-of-mass frame, the net helicity transfer between the ω meson and the photon $|\lambda_\gamma - \lambda_\omega|$ can be 0, 1, or 2, and is referred to as helicity conserving, single- and double-helicity flip, respectively. Both helicity-flip couplings have been fit to SLAC data [13] at an energy of $E_\gamma = 9.3$ GeV and extrapolated to lower energies. The model is shown as the blue curve in Fig. 3. In addition to natural-parity a_2 and f_2 exchanges, as well as unnatural-parity π exchange (naturality given as $\eta = P(-1)^J$ with parity P), natural-parity Pomeron exchange has been considered. The contribution of η exchange is found to be negligible in ω photoproduction and axial-vector trajectories have been neglected in the model [10] since the pseudoscalar exchanges are sufficient to describe the unnatural components of the SDMEs. The model compares well with the two unpolarized SDMEs, ρ_{00}^0 and $\text{Re } \rho_{10}^0$, within its valid range of about $0 < -t < 1 \text{ GeV}^2$, but exhibits the wrong sign for ρ_{1-1}^0 due to an overestimated contribution of unnatural π exchange relative to natural Pomeron and tensor a_2/f_2 exchanges. In the model, a reduction of π exchange would flip the sign of ρ_{1-1}^0 to match data.

The model described in Ref. [32] was developed to analyze the cross sections of meson photo- and electroproduction channels. The red curves in Figs. 2 and 3 show the most recent predictions [33]. In the ϕ channel, the two-gluon exchange contribution reproduces the production cross section [34] and the SDME ρ_{00}^0 at high energy fairly well [35]. In ω production, this contribution is supplemented by π and f_2 exchanges at forward angles, as well as proton exchange at backward angles. While the relativistic spin-momentum dependence of the π exchange amplitude is fully taken into account, the corresponding dependence of the f_2 exchange amplitude is chosen to be the same as that for two-gluon exchange (f_2 -Pomeron equivalence) and, consequently, both conserve helicity. The only difference resides in the propagator: The two-gluon amplitude is purely imaginary (absorptive), whereas the f_2 amplitude is real and incorporates the Regge propagator with the linear trajectory of the f_2 . At intermediate angles, the use of a saturating Regge trajectory for the π meson is necessary to account for previously measured cross sections [9]. As can be seen in Fig. 2, the model agreement with the cross sections is excellent (without any adjustments), especially at the highest energies, where the data seem to indicate the predicted minimum at the most backward angles. In contrast, the new SDMEs reported here are not well described. To improve the model, it will be necessary to go beyond the Pomeron- f_2 equivalence, and take into account the actual spin-momentum structure of the f_2 exchange amplitude. This approach is not expected to change the description of the differential cross sections. Furthermore, a saturating trajectory for the f_2 can be used, at the expense of modifying that for π exchange.

In summary, the first comprehensive data set of photo-production cross sections and (un)polarized SDMEs has been presented for the reaction $\gamma p \rightarrow p\omega$ using circularly polarized tagged photons up to $W = 3.25$ GeV and the CLAS spectrometer at Jefferson Laboratory. The results are given in terms of $\cos \Theta_{\text{c.m.}}^\omega$ for $W \in [1.95, 2.83]$ GeV and in terms of $-t$ for $W \in [2.45, 3.25]$ GeV. We observe excellent agreement with predictions for the cross sections. At the highest energy, the data seem to be consistent with a downward bending at large $| -t |$ values providing a hint for the node predicted by the model in Ref. [33]. Moreover, the new set of SDMEs shows fair agreement with the predictions of the JPAC model [10] for $-t < 1 \text{ GeV}^2$. However, the data indicate that the model significantly overestimates the contribution of unnatural to natural π exchange, which is most obvious for ρ_{1-1}^0 . These new measurements provide a testing ground for the improvements required in the current models. In particular, the first extraction of the polarized SDMEs $\text{Im } \rho_{10}^3$ and $\text{Im } \rho_{1-1}^3$ provides important additional information to improve our understanding of ω photoproduction in the transition from the baryon resonance regime to high-energy photoproduction.

The authors gratefully acknowledge the excellent support of the technical staff at Jefferson Lab and all participating institutions. This research is based on work supported by the U.S. Department of Energy, Office of Science, Office of Nuclear Physics, under Contract No. DE-AC05-06OR23177. The group at Florida State University acknowledges additional support from the U.S. Department of Energy, Office of Science, Office of Nuclear Physics, under Contract No. DE-FG02-92ER40735. This work was also supported by the U.S. National Science Foundation, the State Committee of Science of Republic of Armenia, the Italian Istituto Nazionale di Fisica Nucleare, the French Centre National de la Recherche Scientifique, the French Commissariat à l'Energie Atomique, the Scottish Universities Physics Alliance (SUPA), the United Kingdom Science and Technology Facilities Council (STFC), the National Research Foundation of Korea, the Deutsche Forschungsgemeinschaft (SFB/TR110), the Russian Science Foundation under Grant No. 16-12-10267, the National Natural Science Foundation of China under Grants No. 11475181 and No. 11635009, and in part by the Chilean National Agency of Research and Development ANID PIA/APOYO AFB180002. V. Mathieu is a Serra Húnter fellow and acknowledges support from the Spanish national Grant No. PID2019-106080 GB-C21 and PID2020-118758GB-I00.

-
- [16] D. P. Barber *et al.* [LAMP2 Group], *Z. Phys. C* **26**, 343 (1984).
 - [17] H. R. Crouch *et al.*, *Phys. Rev.* **146**, 994 (1966).
 - [18] R. Erbe *et al.* [ABBHHM Collaboration], *Phys. Rev.* **175**, 1669 (1968).
 - [19] M. Battaglieri *et al.* [CLAS Collaboration], *Phys. Rev. Lett.* **90**, 022002 (2003).
 - [20] M. Williams *et al.* [CLAS Collaboration], *Phys. Rev. C* **80**, 065208 (2009).
 - [21] T. Hu *et al.* [CLAS Collaboration], *Phys. Rev. C* **102**, no.6, 065203 (2020).
 - [22] Z. Akbar, Ph.D. thesis, Florida State University, 2018.
 - [23] H. Olsen and L. C. Maximon, *Phys. Rev.* **114**, 887 (1959).
 - [24] D. I. Sober *et al.*, *Nucl. Instrum. Meth. A* **440**, 263 (2000).
 - [25] B. A. Mecking *et al.*, *Nucl. Instrum. Meth. A* **503**, 513 (2003).
 - [26] P. A. Zyla *et al.* [Particle Data Group], *PTEP* **2020**, no.8, 083C01 (2020).
 - [27] M. Williams, M. Bellis and C. A. Meyer, *JINST* **4**, P10003 (2009).
 - [28] R. Brun, F. Bruyant, F. Carminati, S. Giani, M. Maire, A. McPherson, G. Patrick and L. Urban, doi:10.17181/CERN.MUHF.DMJ1.
 - [29] See Supplemental Material at [URL will be inserted by publisher] for the full set of differential cross sections (including tables with numerical values) $d\sigma/d(\cos\Theta)$ in 20-MeV-wide and 10-MeV-wide bins for the W range 1.95–2.35 GeV and 2.35–2.83 GeV, respectively, and $d\sigma/dt$ in 20-MeV-wide energy bins for the W range 2.45–3.25 GeV.
 - [30] CLAS-g12 Run Group, CLAS-NOTE 2017-002, 2017, <https://misportal.jlab.org/u1/Physics/Hall-B/clas/viewFile.cfm/2017-002?documentId=756>.
 - [31] See Supplemental Material at [URL will be inserted by publisher] for the full set of spin-density elements (including tables with numerical values), ρ_{00}^0 , ρ_{1-1}^0 , $\text{Re } \rho_{10}^0$ and $\text{Im } \rho_{10}^3$, $\text{Im } \rho_{1-1}^3$, in 20-MeV-wide energy bins for the W range 2.45–3.25 GeV.
 - [32] J. M. Laget, *Prog. Part. Nucl. Phys.* **111**, 103737 (2020).
 - [33] J. M. Laget, *Phys. Rev. C* **104**, no.2, 025202 (2021).
 - [34] E. Anciant *et al.* [CLAS Collaboration], *Phys. Rev. Lett.* **85**, 4682 (2000).
 - [35] K. McCormick *et al.* [CLAS Collaboration], *Phys. Rev. C* **69**, 032203 (2004).

* Present address: University of Virginia, Charlottesville, Virginia 22901, USA

† Corresponding author: crede@fsu.edu

‡ Current address: Idaho State University, Pocatello, Idaho 83209, USA

- [1] Z. Akbar *et al.* [CLAS Collaboration], *Phys. Rev. C* **96**, 065209 (2017).
- [2] P. Roy *et al.* [CLAS Collaboration], *Phys. Rev. C* **97**, 055202 (2018).
- [3] P. Roy *et al.* [CLAS Collaboration], *Phys. Rev. Lett.* **122**, 162301 (2019).
- [4] N. C. Wei, F. Huang, K. Nakayama and D. M. Li, *Phys. Rev. D* **100**, 114026 (2019).
- [5] A. Wilson *et al.* [CBELSA/TAPS Collaboration], *Phys. Lett. B* **749**, 407 (2015).
- [6] F. Klein *et al.* [CBELSA/TAPS Collaboration], *Phys. Rev. D* **78**, 117101 (2008).
- [7] H. Eberhardt *et al.*, *Phys. Lett. B* **750**, 453 (2015).
- [8] P. D. B. Collins and P. J. Kearney, *Z. Phys. C* **22**, 277 (1984).
- [9] F. Cano and J. M. Laget, *Phys. Rev. D* **65**, 074022 (2002).
- [10] V. Mathieu *et al.* [JPAC Collaboration], *Phys. Rev. D* **97**, 094003 (2018).
- [11] K. Schilling, P. Seyboth and G. E. Wolf, *Nucl. Phys. B* **15**, 397 (1970) [erratum: *Nucl. Phys. B* **18**, 332 (1970)].
- [12] J. Ballam *et al.*, *Phys. Rev. Lett.* **24**, 1364 (1970).
- [13] J. Ballam *et al.*, *Phys. Rev. D* **7**, 3150 (1973).
- [14] J. Abramson *et al.*, *Phys. Rev. Lett.* **36**, 1428 (1976).
- [15] R. W. Clift *et al.*, *Phys. Lett. B* **72**, 144 (1977).

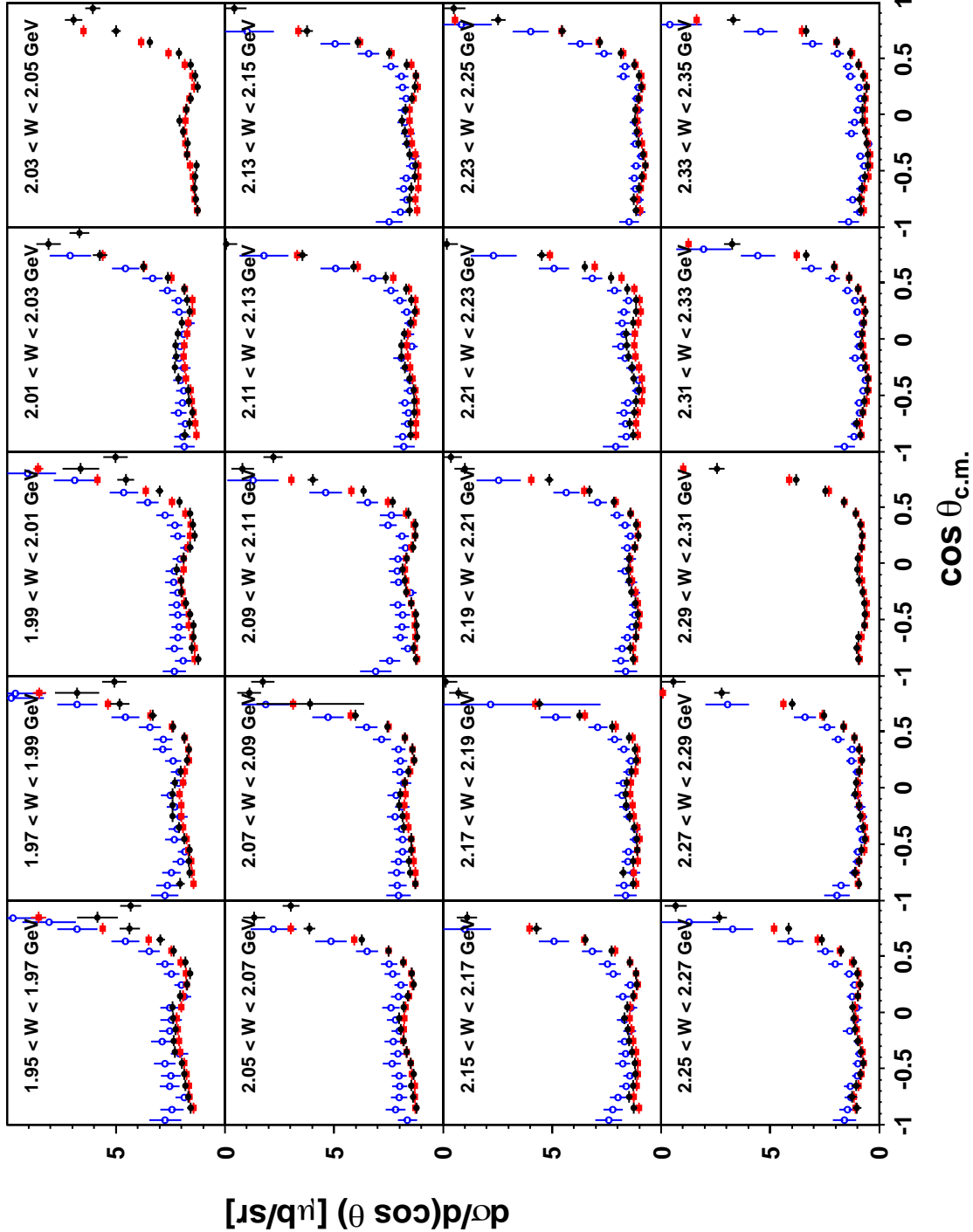


FIG. 5. The differential cross sections $d\sigma/d(\cos \Theta)$ in 20-MeV-wide center-of-mass bins for $W \in [1.95, 2.35]$ GeV. The new CLAS data are shown as the black solid circles (●) and the uncertainties associated with each point comprise the statistical uncertainty and contributions from the Q -value correlation uncertainty added in quadrature. Also shown for comparison are earlier data from the CLAS-g11a experiment [20] (■) and CBELSA/TAPS [5] (○).

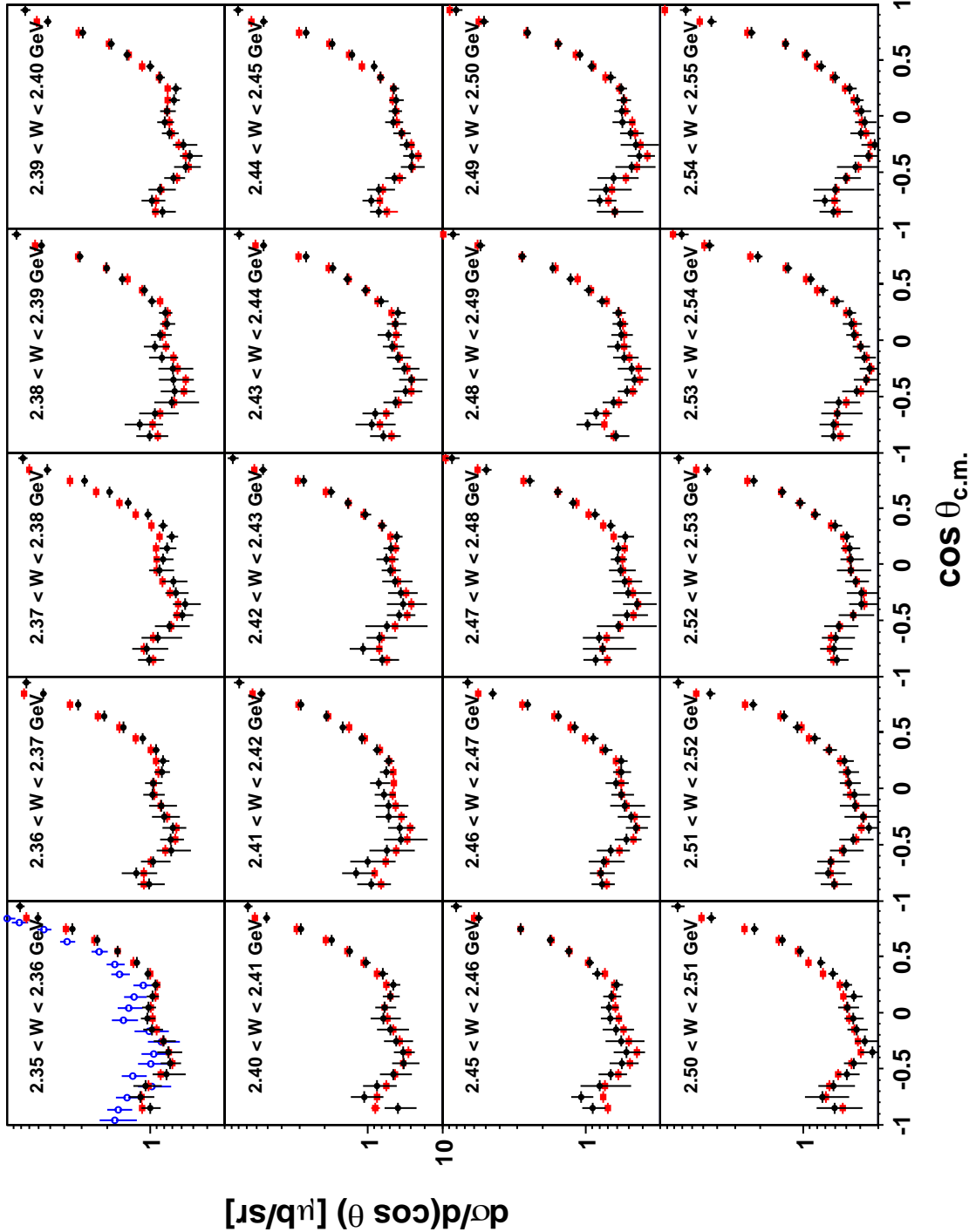


FIG. 6. The differential cross sections $d\sigma/d(\cos \Theta)$ in 10-MeV-wide center-of-mass bins for $W \in [2.35, 2.55]$ GeV. The new CLAS data are shown as the black solid circles (●) and the uncertainties associated with each point comprise the statistical uncertainty and contributions from the Q -value correlation uncertainty added in quadrature. Also shown for comparison are earlier data from the CLAS-g11a experiment [20] (■) and CBELSA/TAPS [5] (○).

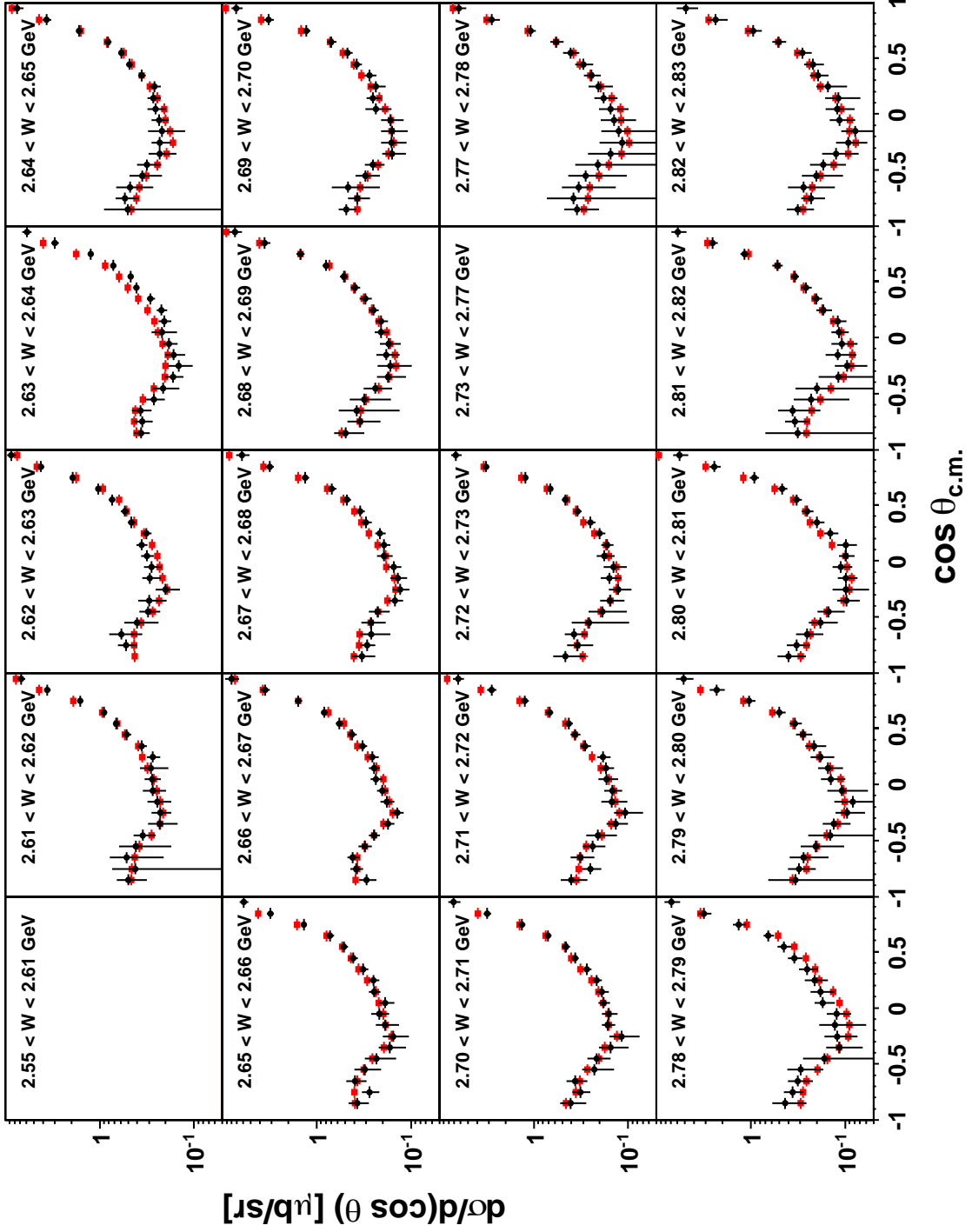


FIG. 7. The differential cross sections $d\sigma/d(\cos \Theta)$ in 10-MeV-wide center-of-mass bins for $W \in [2.55, 2.83]$ GeV. The new CLAS data are shown as the black solid circles (●) and the uncertainties associated with each point comprise the statistical uncertainty and contributions from the Q -value correlation uncertainty added in quadrature. CLAS-g11 data are not available for the energy bin $2.56 < W < 2.61$ GeV, caused by an established tagger inefficiency in the detectors of the target focal plane in this region. Also shown for comparison are earlier data from the CLAS-g11a experiment [20] (■).

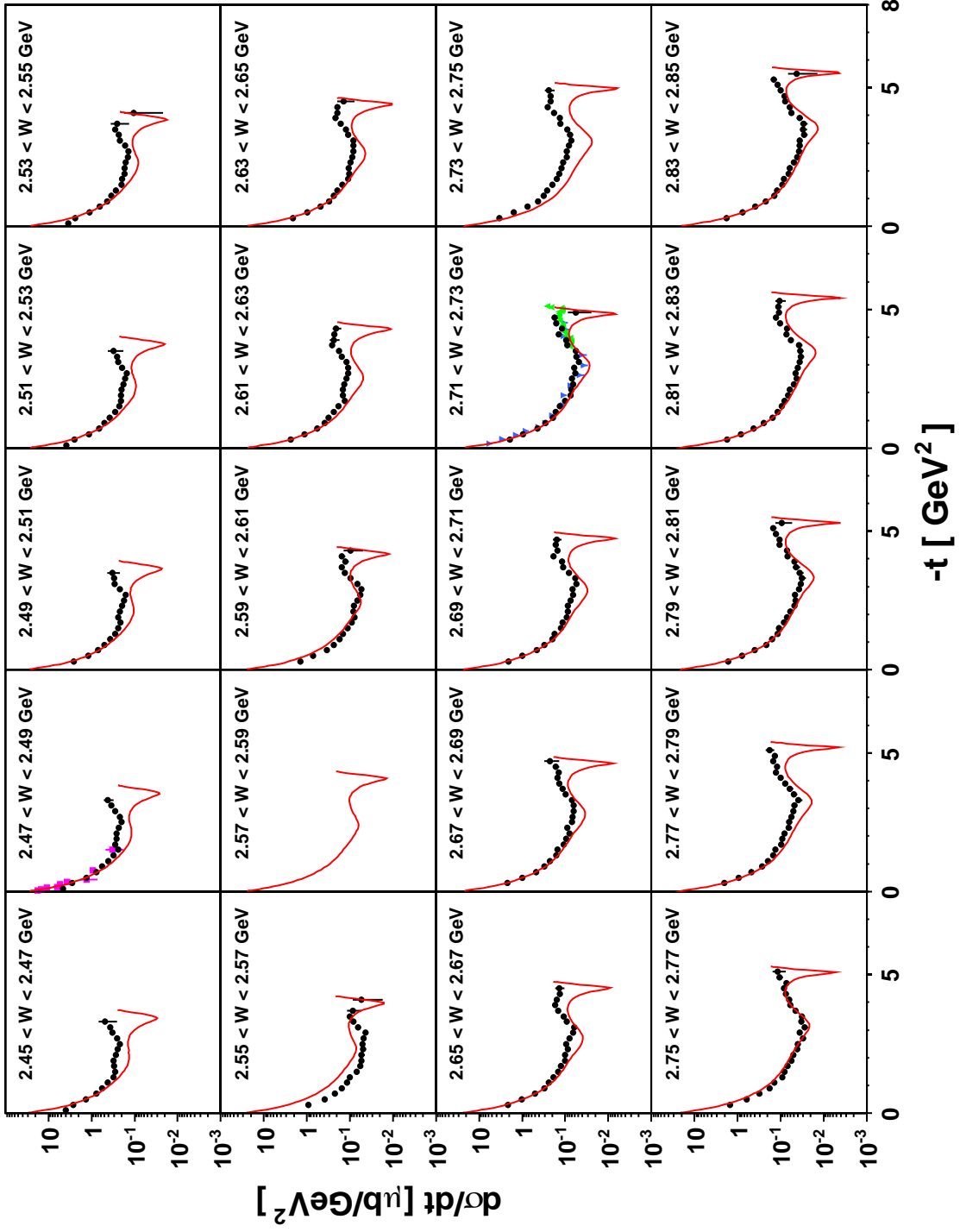


FIG. 8. The differential cross sections $d\sigma/dt$ in 20-MeV-wide center-of-mass bins for $W \in [2.45, 2.85]$ GeV. The new CLAS data are shown as the black solid circles (\bullet) and the uncertainties associated with each point comprise the statistical uncertainty and contributions from the Q -value correlation uncertainty added in quadrature. CLAS-g12 data are not available for the energy bin $2.56 < W < 2.61$ GeV, caused by an established tagger inefficiency in the detectors of the tagger focal plane in this region. Also shown for comparison are earlier data from CLAS [19] (\blacktriangle) for the energy bin $E_\gamma \in [3.38, 3.56]$ GeV, NINA [15] (\blacktriangle) at $E_\gamma = 3.5$ GeV, and SLAC [13] (\blacksquare) at $E_\gamma = 2.8$ GeV. The red curves denote the model predictions of Ref. [33].

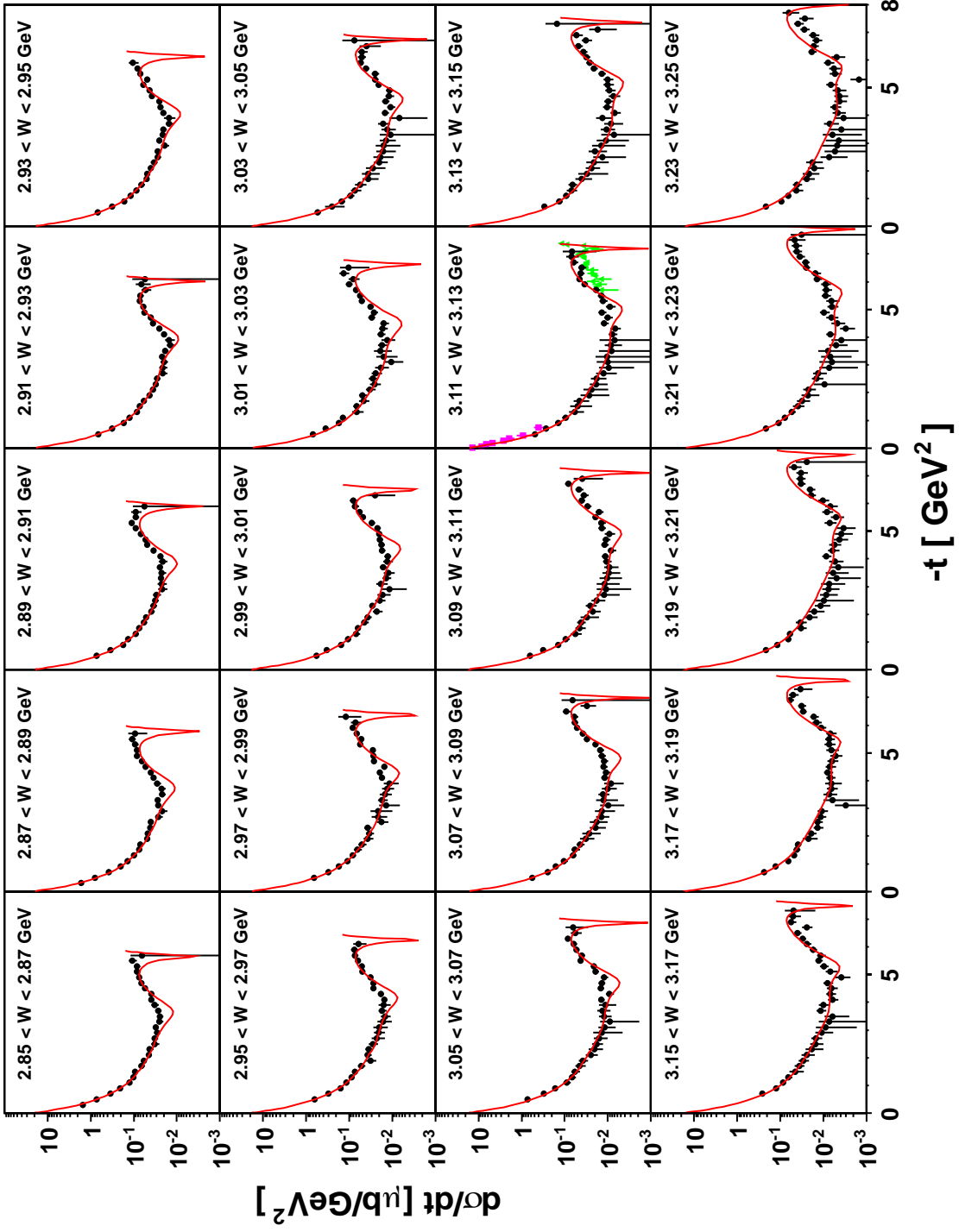


FIG. 9. The differential cross sections $d\sigma/dt$ in 20-MeV-wide center-of-mass bins for $W \in [2.85, 3.25]$ GeV. The new CLAS data are shown as the black solid circles (\bullet) and the uncertainties associated with each point comprise the statistical uncertainty and contributions from the Q -value correlation uncertainty added in quadrature. Also shown for comparison are data from NINA [15] (\blacktriangle) at $E_\gamma = 4.7$ GeV and SLAC [13] (\blacksquare) at $E_\gamma = 4.7$ GeV. The red curves denote the model predictions of Ref. [33].

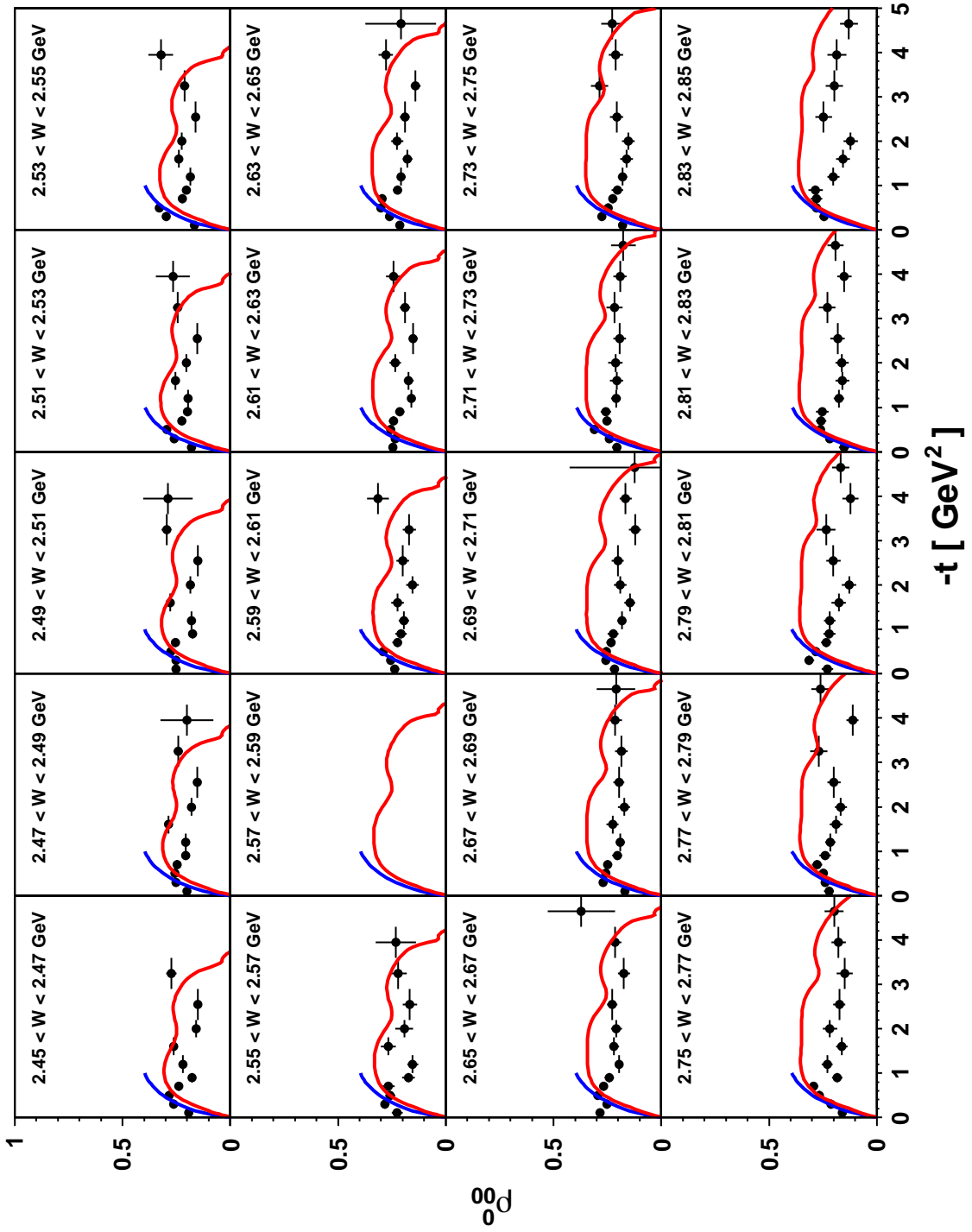


FIG. 10. The unpolarized spin-density matrix element ρ_{00}^0 in 20-MeV-wide center-of-mass bins for $W \in [2.45, 2.85]$ GeV in the helicity frame. The blue solid curves denote the model prediction of Ref. [10] and the red curves denote the model predictions of Ref. [33].

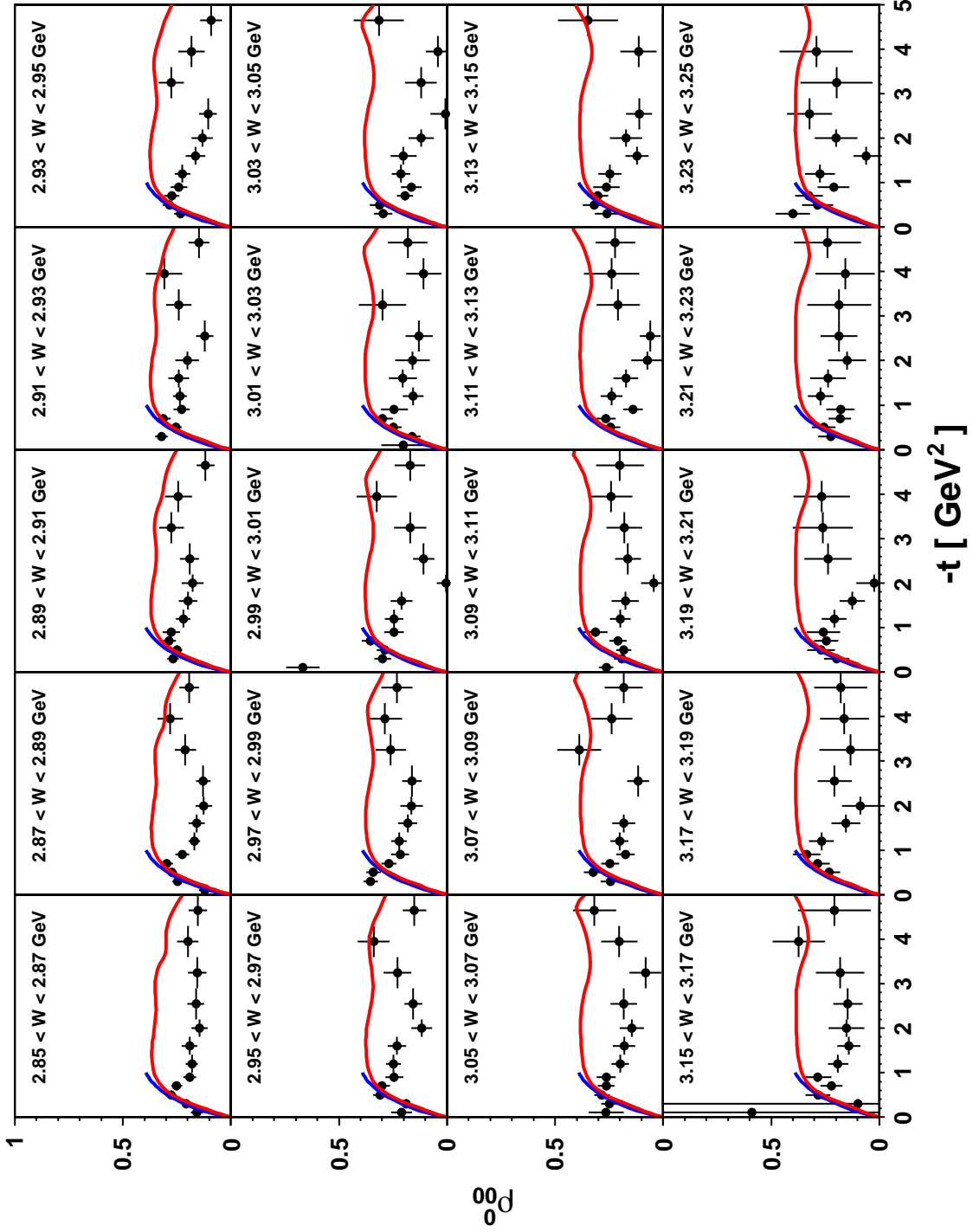


FIG. 11. The unpolarized spin-density matrix element ρ_{00}^0 in 20-MeV-wide center-of-mass bins for $W \in [2.85, 3.25] \text{ GeV}$ in the helicity frame. The blue solid curves denote the model prediction of Ref. [10] and the red curves denote the model predictions of Ref. [33].

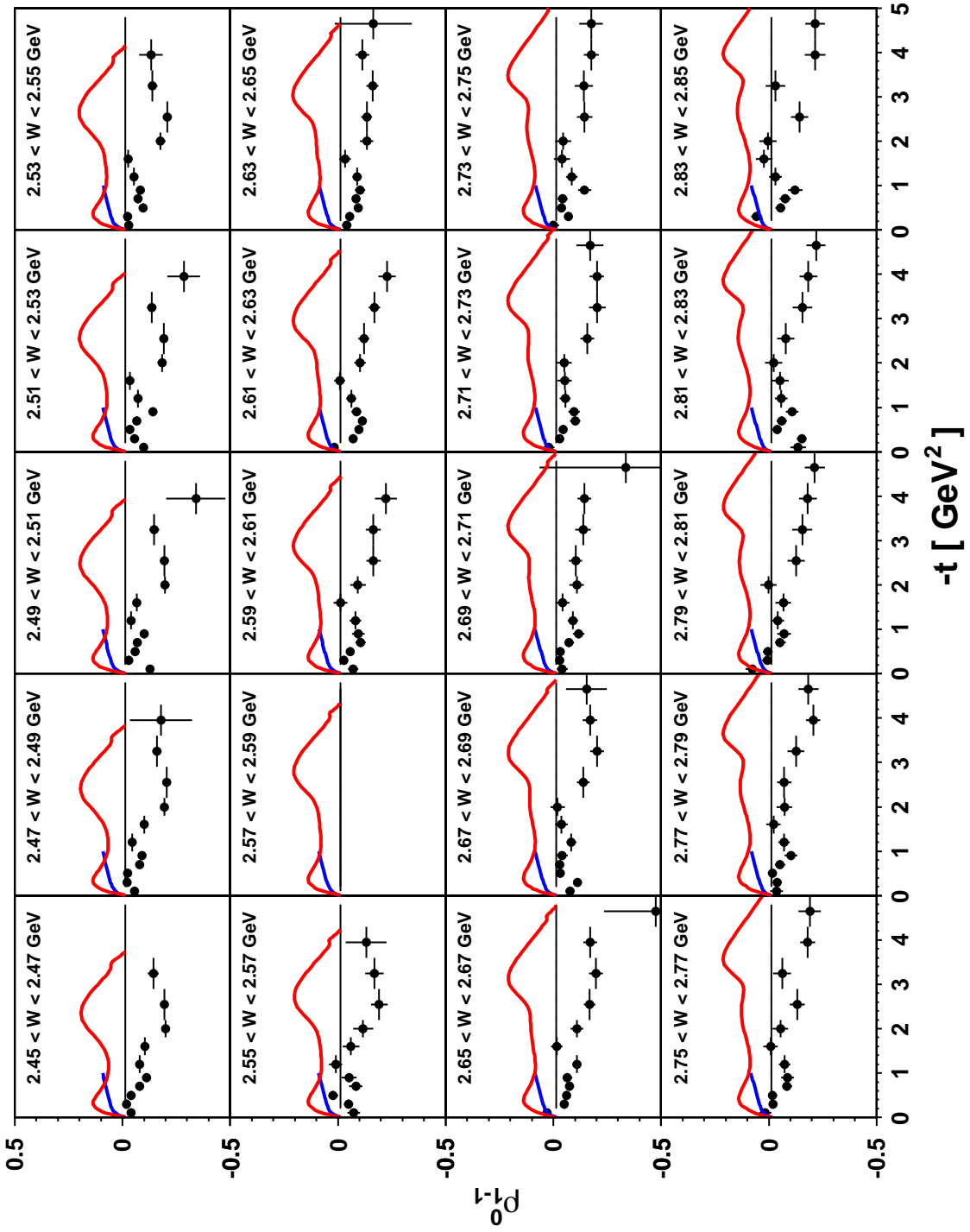


FIG. 12. The unpolarized spin-density matrix element ρ_{1-1}^0 in 20-MeV-wide center-of-mass bins for $W \in [2.45, 2.85]$ GeV in the helicity frame. The blue solid curves denote the model prediction of Ref. [10] and the red curves denote the model predictions of Ref. [33].

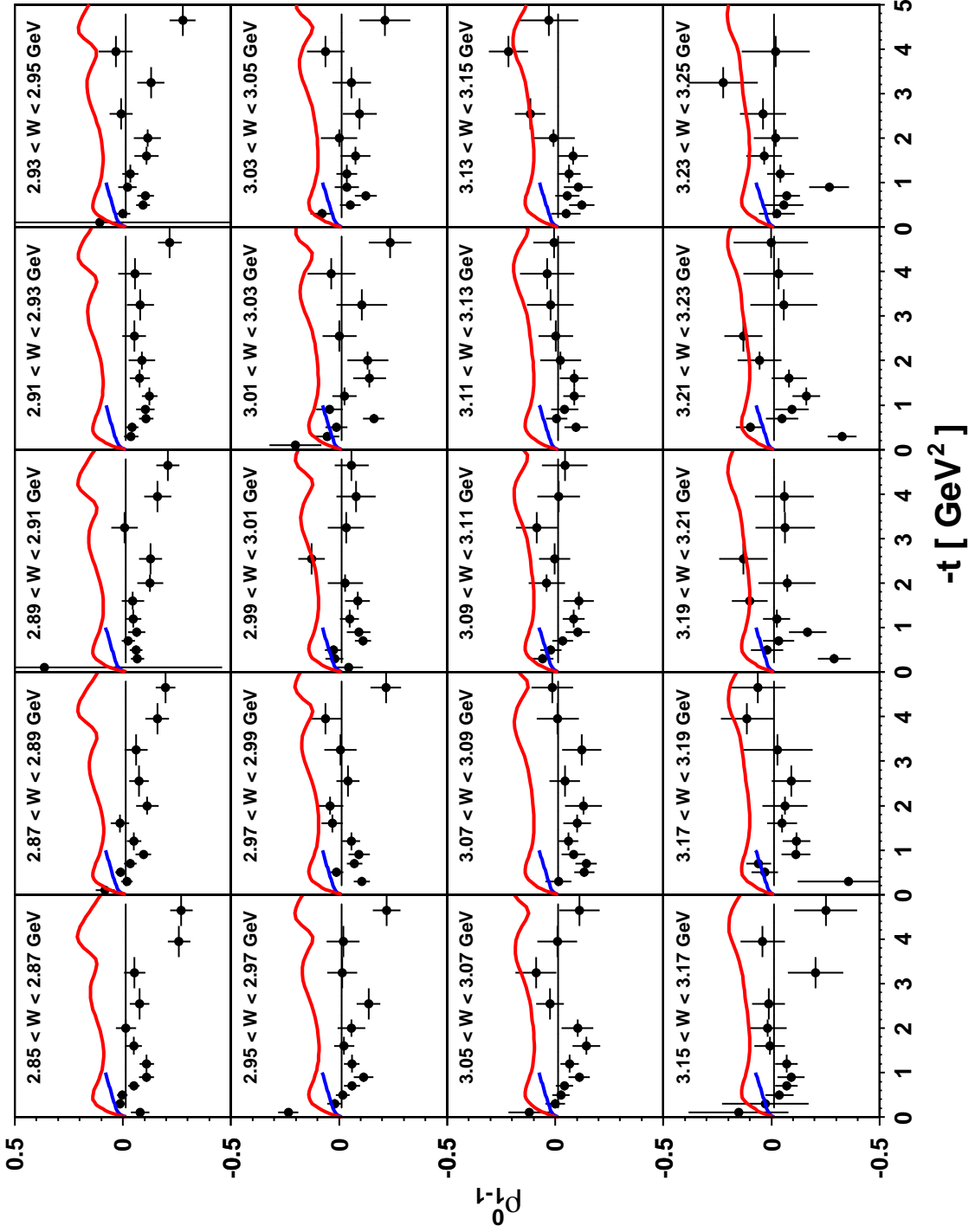


FIG. 13. The unpolarized spin-density matrix element ρ_{1-1}^0 in 20-MeV-wide center-of-mass bins for $W \in [2.85, 3.25]$ GeV in the helicity frame. The blue solid curves denote the model prediction of Ref. [10] and the red curves denote the model predictions of Ref. [33].

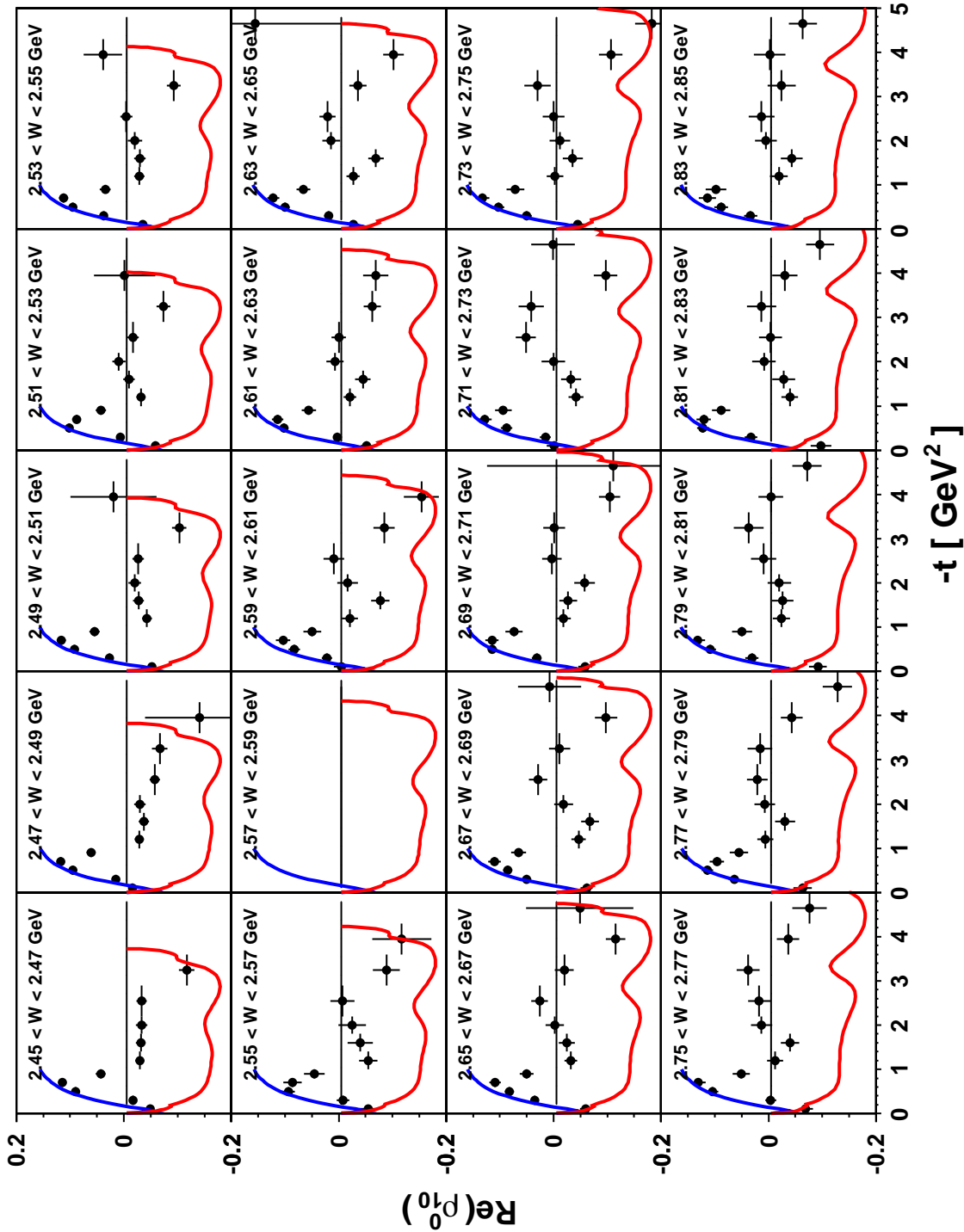


FIG. 14. The unpolarized spin-density matrix element $\text{Re} \rho_{10}^0$ in 20-MeV-wide center-of-mass bins for $W \in [2.45, 2.85]$ GeV in the helicity frame. The blue solid curves denote the model prediction of Ref. [10] and the red curves denote the model predictions of Ref. [33].

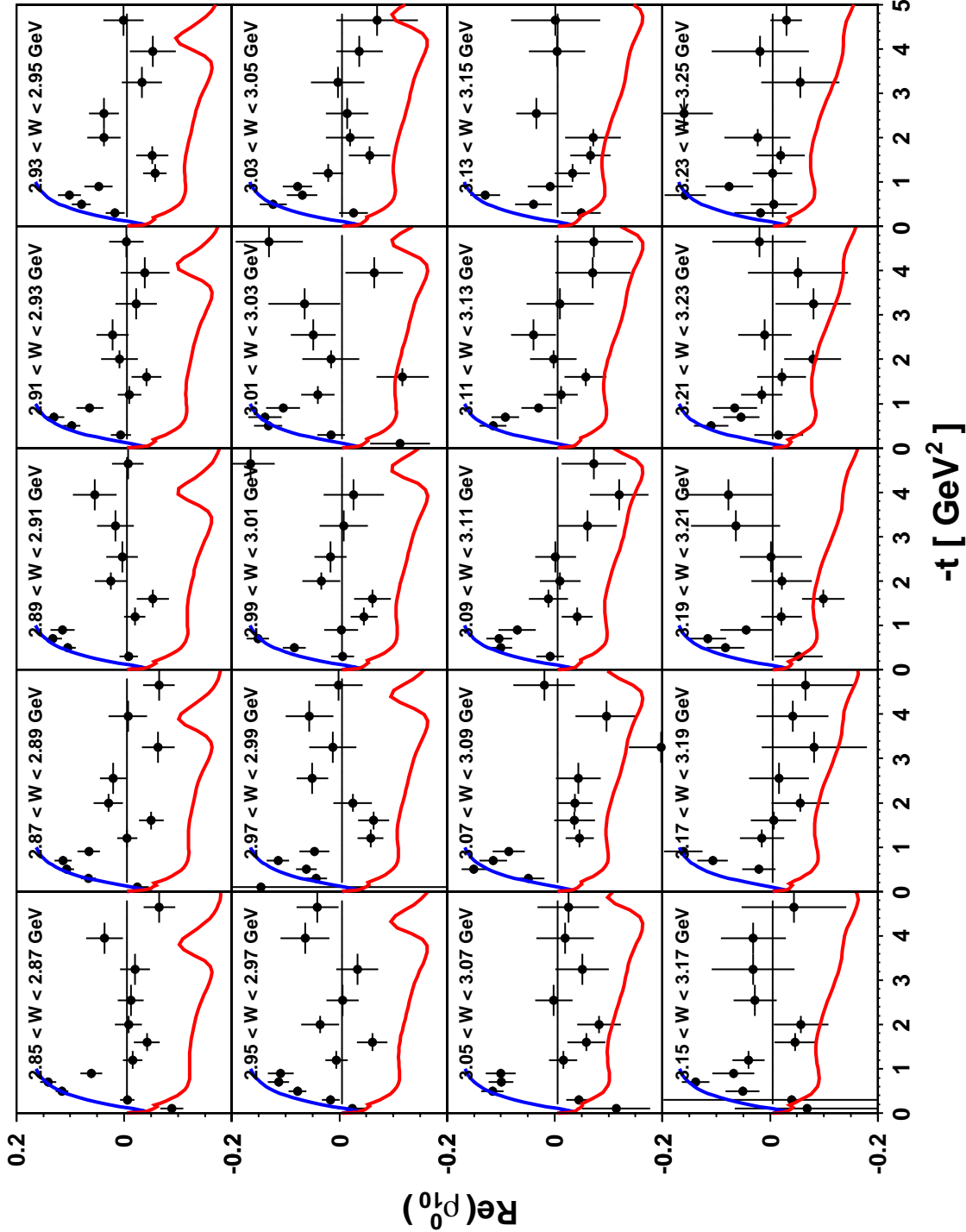


FIG. 15. The unpolarized spin-density matrix element $\text{Re} \rho_{10}^0$ in 20-MeV-wide center-of-mass bins for $W \in [2.85, 3.25]$ GeV in the helicity frame. The blue solid curves denote the model prediction of Ref. [10] and the red curves denote the model predictions of Ref. [33].

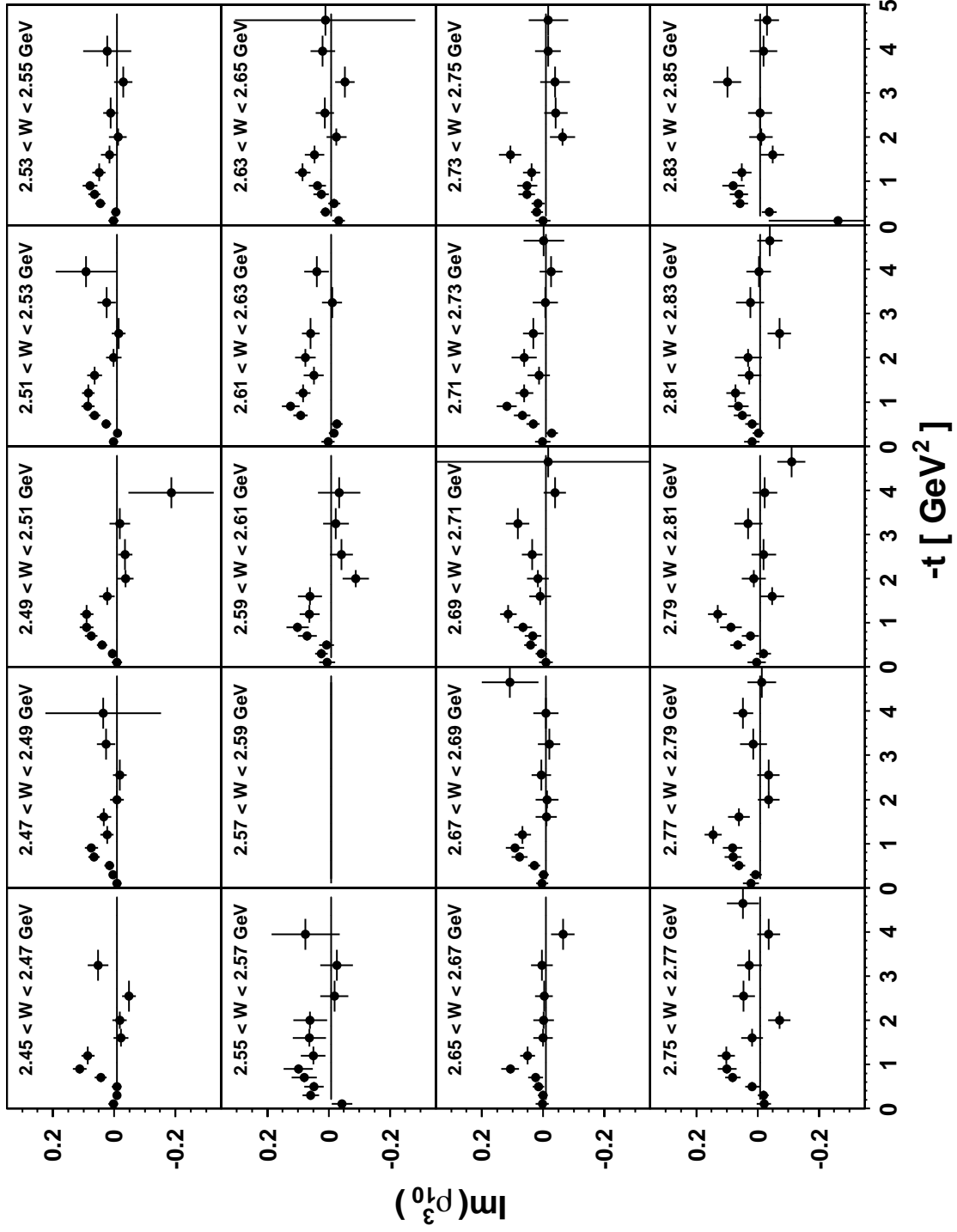


FIG. 16. The polarized spin-density matrix element $\text{Im} \rho_{01}^3$ in 20-MeV-wide center-of-mass bins for $W \in [2.45, 2.85]$ GeV in the helicity frame.

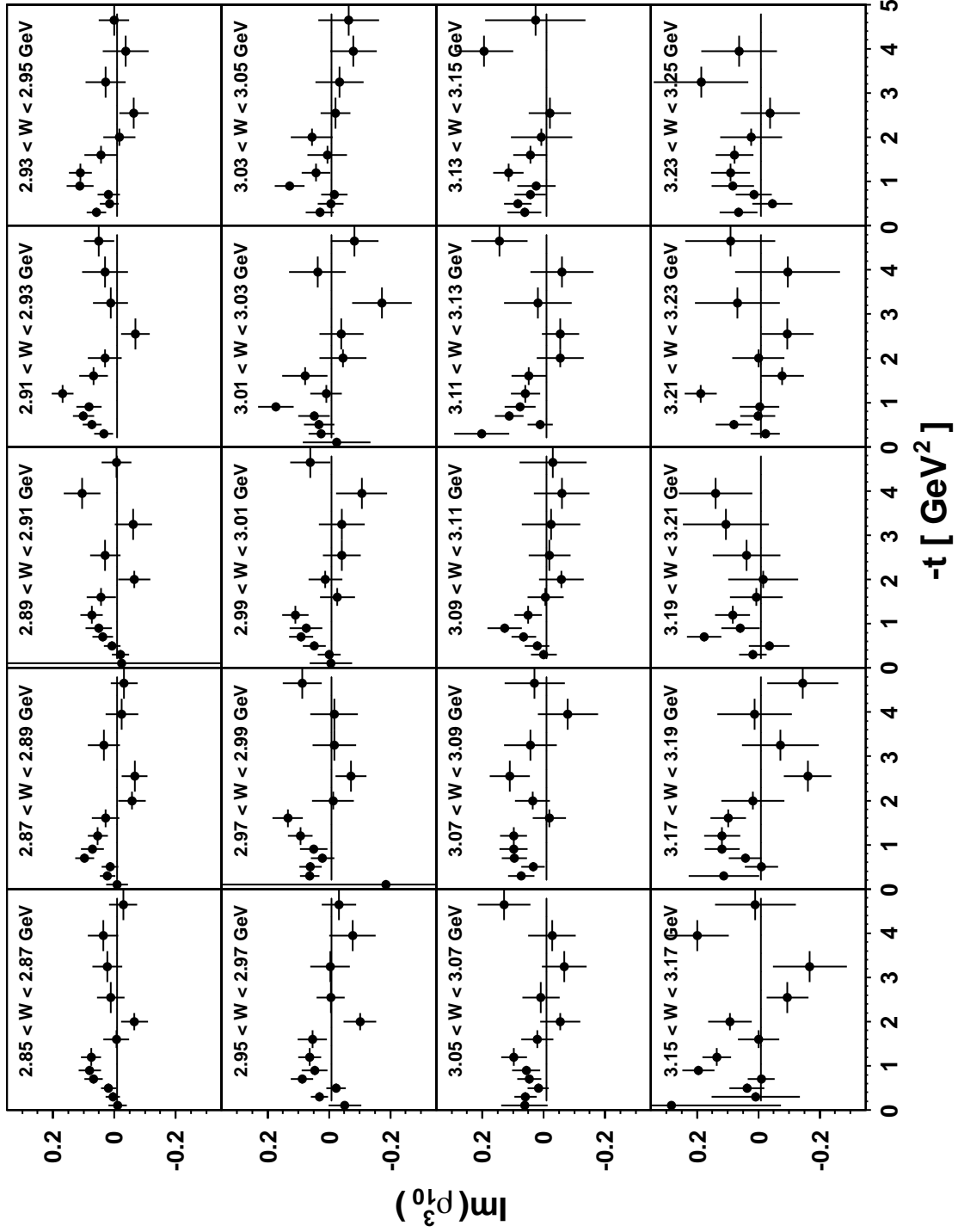


FIG. 17. The polarized spin-density matrix element $\text{Im} \rho_{10}^3$ in 20-MeV-wide center-of-mass bins for $W \in [2.85, 3.25]$ GeV in the helicity frame.

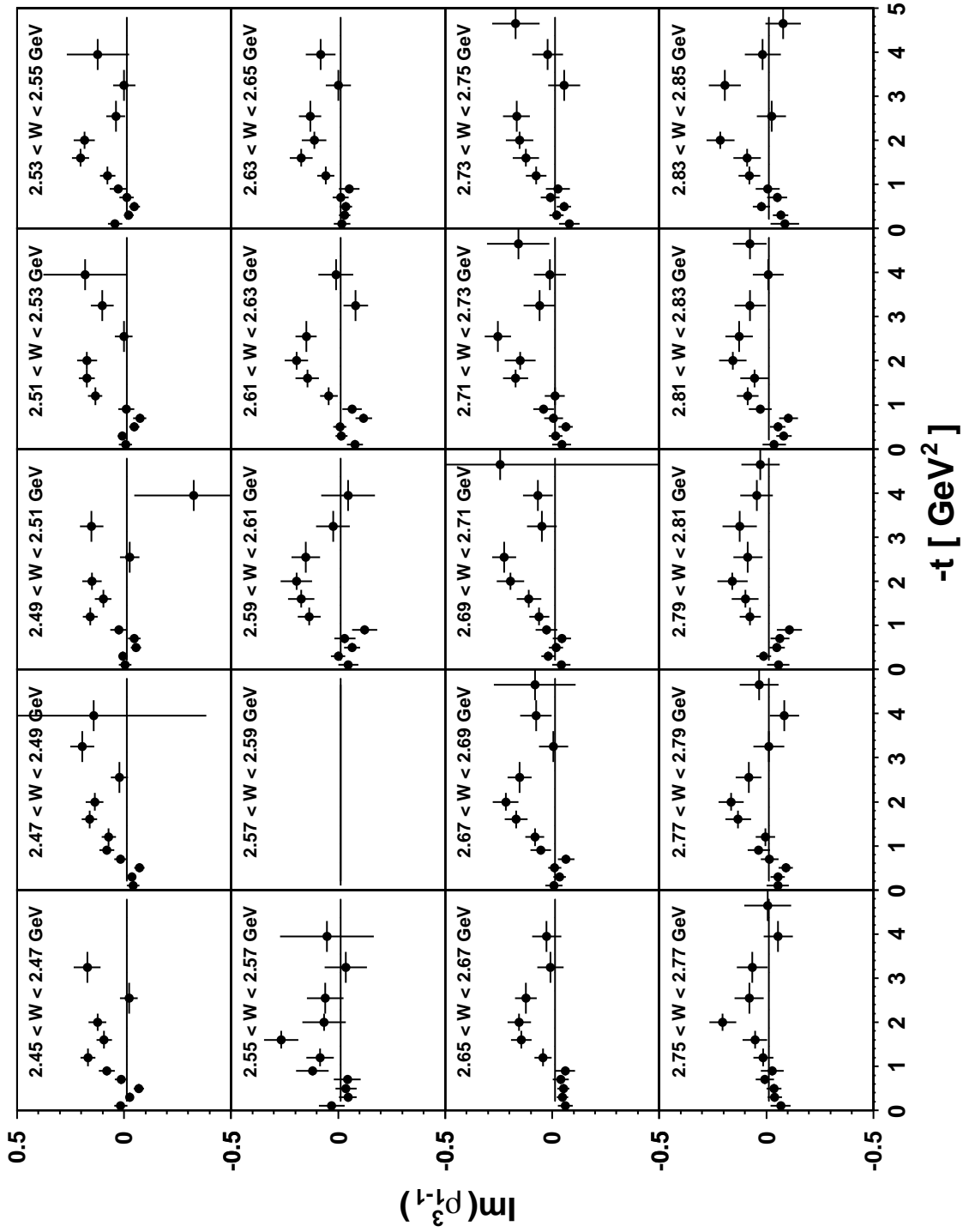


FIG. 18. The polarized spin-density matrix element $\text{Im} \rho_{1-1}^3$ in 20-MeV-wide center-of-mass bins for $W \in [2.45, 2.85]$ GeV in the helicity frame.

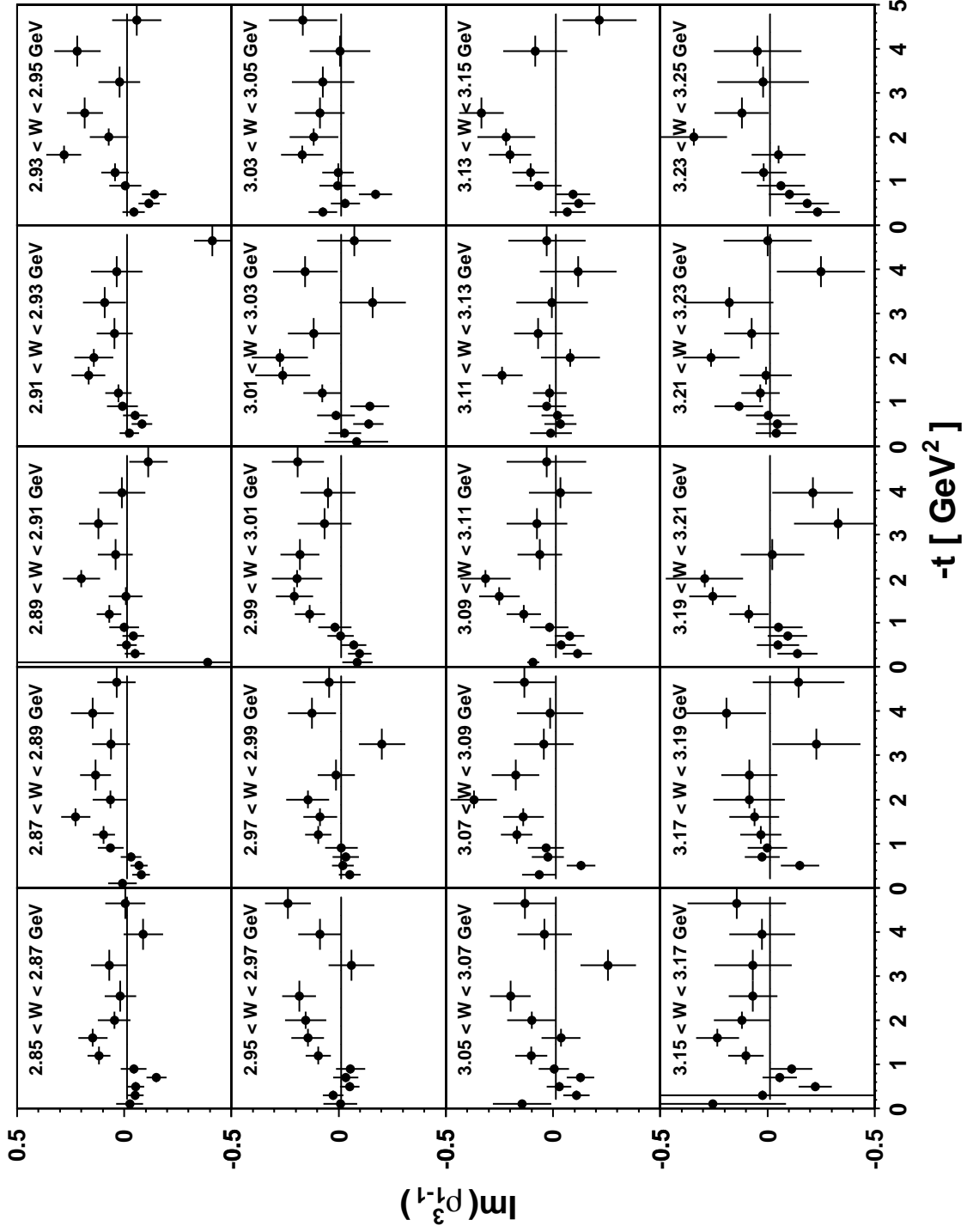


FIG. 19. The polarized spin-density matrix element $\text{Im} \rho_{1-1}^3$ in 20-MeV-wide center-of-mass bins for $W \in [2.85, 3.25]$ GeV in the helicity frame.

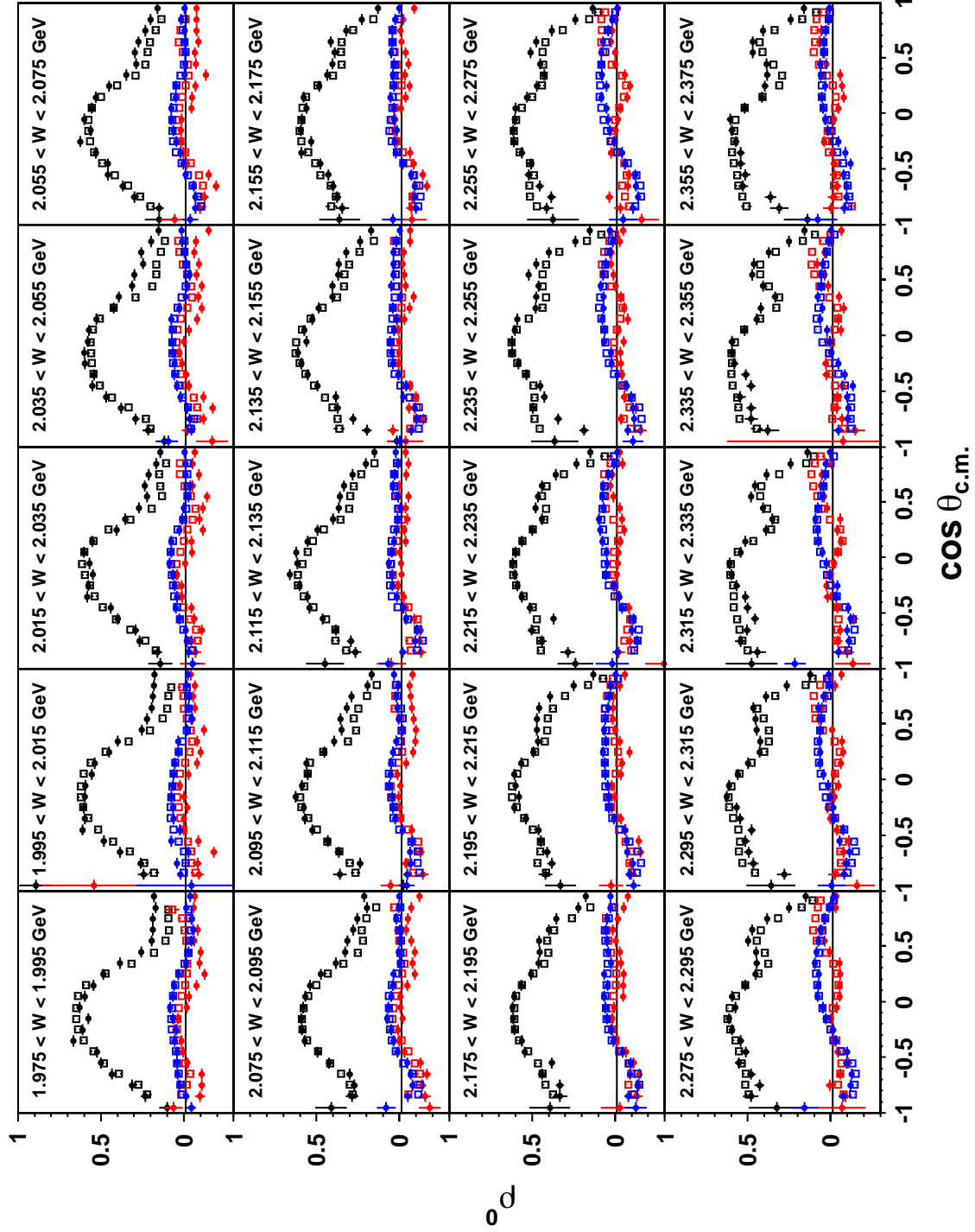


FIG. 20. The unpolarized spin-density matrix elements ρ_{00}^0 , ρ_{1-1}^0 , and $\text{Re } \rho_{10}^0$ in 20-MeV-wide center-of-mass bins for $W \in [1.975, 2.375]$ GeV in the Adair frame. The new CLAS data are shown as the black solid circles (\bullet) and the uncertainties associated with each point comprise the statistical uncertainty and contributions from the Q -value correlation uncertainty added in quadrature. Also shown for comparison are earlier data from the CLAS-g11a experiment [20] as the corresponding open symbols.

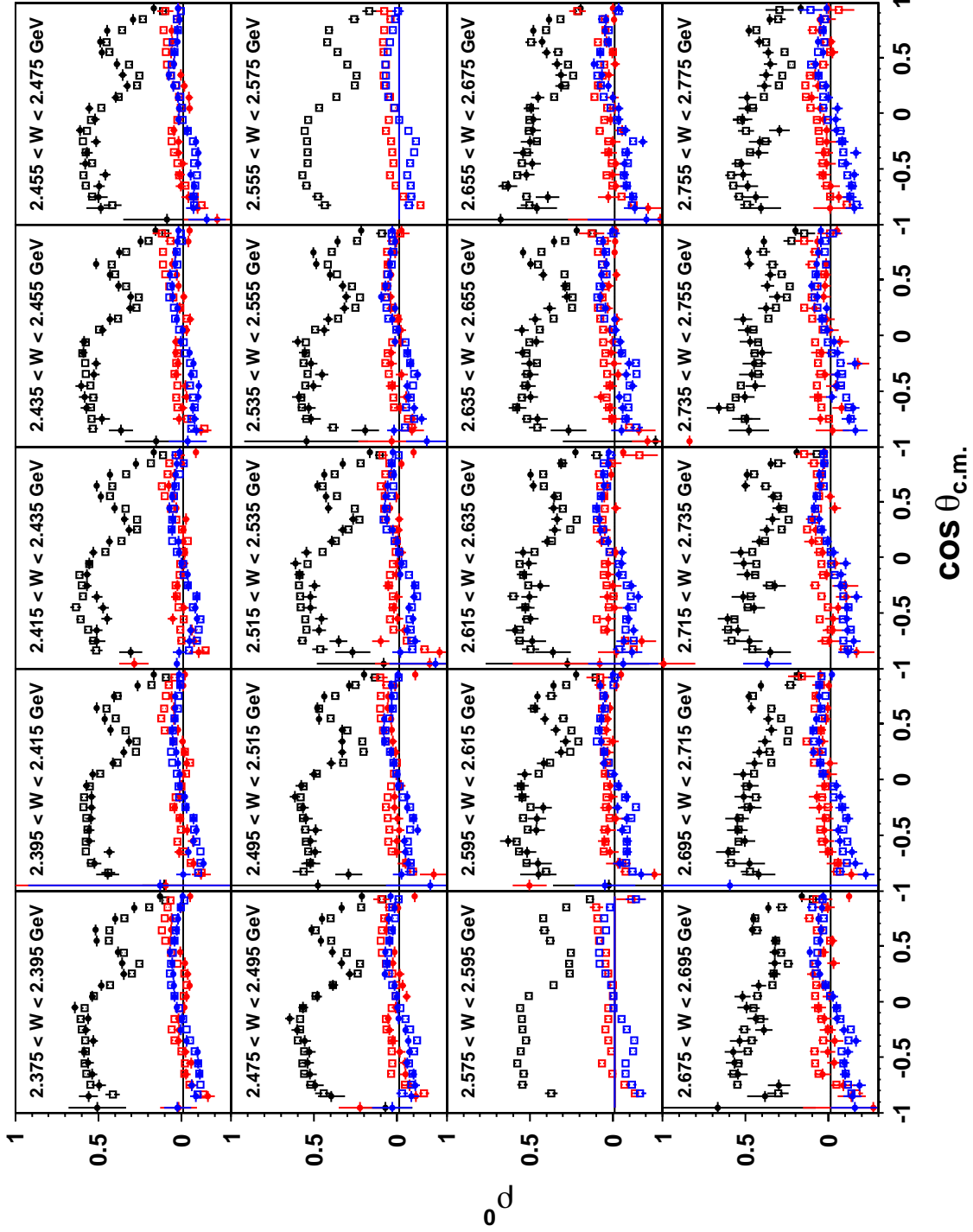


FIG. 21. The unpolarized spin-density matrix elements ρ_{00}^0 , ρ_{1-1}^0 , and $\text{Re } \rho_{10}^0$ in 20-MeV-wide center-of-mass bins for $W \in [2.375, 2.775]$ GeV in the Adair frame. The new CLAS data are shown as the black solid circles (\bullet) and the uncertainties associated with each point comprise the statistical uncertainty and contributions from the Q -value correlation uncertainty added in quadrature. Also shown for comparison are earlier data from the CLAS-g1a experiment [20] as the corresponding open symbols.